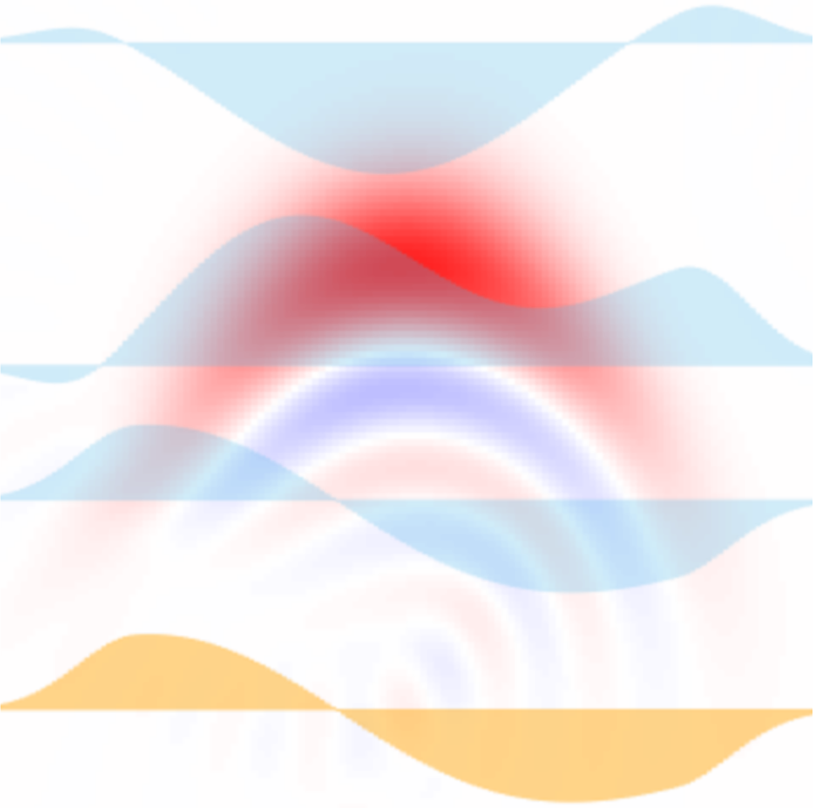

Optimal Control of a SNAIL-resonator

Master's thesis in Physics

NILS NERPIN

DEPARTMENT OF MICROTECHNOLOGY AND NANOSCIENCE
CHALMERS UNIVERSITY OF TECHNOLOGY
Gothenburg, Sweden 2025
www.chalmers.se

MASTER'S THESIS 2025

Optimal Control of a SNAIL-resonator

NILS NERPIN

Department of Microtechnology and Nanoscience
Division of Applied Quantum Physics
CHALMERS UNIVERSITY OF TECHNOLOGY
Gothenburg, Sweden 2025

Optimal Control of a SNAIL-resonator
NILS NERPIN

Supervisor: Tahereh Abad, Department of Microtechnology and Nanoscience
Examiner: Göran Johansson, Department of Microtechnology and Nanoscience

Master's Thesis 2025
Department of Microtechnlogy and Nanoscience
Division of Applied Quantum Physics
Chalmers University of Technology
SE-412 96 Gothenburg
Telephone +46 31 772 1000

Cover: Wigner distribution of a cubic phase state generated by optimal control pulses.

Typeset in LaTeX
Printed by Chalmers Reproservice
Gothenburg, Sweden 2025

Optimal Control of a SNAIL-resonator
NILS NERPIN
Department of Microtechnology and Nanoscience
Chalmers University of Technology

Abstract

In recent experiments done at Chalmers, universal control of a bosonic mode was demonstrated for a superconducting cavity terminated by a Superconducting Nonlinear Asymmetric Inductive eLement (SNAIL), while simultaneously cancelling Kerr effects by applying an external magnetic flux to the SNAIL. The universal control was demonstrated by generating a cubic phase state; however, generating other interesting non-Gaussian states remains a non-trivial issue. The aim of this work is to perform optimal control on the SNAIL-resonator. Due to the large Hilbert space of the system and its fast time dependence, an effective Hamiltonian is derived from the previously known full Hamiltonian in the regime of resonant driving, which significantly speeds up the optimization process. The drives of the system are then optimized to reach a target cubic phase state, both by simply tuning the amplitudes and phases of the pulses used in the Chalmers experiment and by pulse shaping optimization. Then, optimal control is used to generate two-photon cat states. The results are analyzed in terms of the fidelity to target states and its susceptibility to circuit parameter deviations. Finally, the potential for using optimal control to find experimentally viable methods of generating non-Gaussian states is discussed.

Keywords: Quantum computing, bosonic modes, universal control, superconducting, effective Hamiltonian, optimal control.

Acknowledgements

First and foremost, I would like to thank my supervisor, Tahereh Abad, for giving me the opportunity to work on this project and for her invaluable guidance and support throughout. I would also like to thank Axel Eriksson and Martin Jirlow for the many discussions that have helped shape this work. Furthermore, I want to thank Théo Sépulcre, Giulia Ferrini, and Alessandro Ferraro for sharing their ideas on the project. I would also like to thank Göran Johansson for serving as my examiner, and Joel Sandås for taking the time to be my opponent. Finally, I am deeply thankful to my partner, family, and friends for their endless support, both during this project and in life in general.

Nils Nerpin, Gothenburg, July 2025

List of Acronyms

Below is the list of acronyms that have been used throughout this intermediate report listed in alphabetical order:

ATS	Asymmetrically Threaded Superconducting quantum interference device
CV	Continuous Variable
cQED	Circuit Quantum Electrodynamics
GKP	Gottesman-Kitaev-Preskill
JJ	Josephson Junction
RWA	Rotating Wave Approximation
SNAIL	Superconducting Nonlinear Asymmetric Inductive eLement

Contents

List of Figures

List of Tables

1

Introduction

The purpose of a quantum computer is to harness the intrinsic properties of quantum mechanics to solve problems that are inefficient to solve on classical computers. Today, there are multiple proposed platforms for building such computers, such as trapped ions [1] and quantum dot spin systems [2]. Another method is to use macroscopic quantum mechanical effects in superconducting circuits [3], which is considered in this work.

The most common approach to this is coupling multiple superconducting qubits, where the information is encoded in each qubit as a superposition of a two-level system [4]. An alternative approach is to encode the information in bosonic modes instead [5], [6], also referred to as Continuous Variable (CV) quantum computing. Here, the quantum information can be protected against errors by making use of the large Hilbert space [7], [8]. In superconducting circuits, universal control of this mode can be achieved by dispersively coupling a cavity to a qubit [9]–[11]. However, the fidelity of operations is limited, as the setup inherently comes with a Kerr nonlinearity [12].

Recently, universal control of a bosonic mode was demonstrated experimentally in [13] after being theoretically proposed in [14]. This was done by terminating a $\lambda/4$ resonator with a Superconducting Nonlinear Asymmetric Inductive eLement (SNAIL) [15], and then controlling the mode by driving the resonator through a transmission line and tuning the SNAIL through a flux pump. This tuning allows for canceling Kerr effects by applying a static, external magnetic flux. Notably, the architecture was used to generate a cubic phase state, with an estimated fidelity to the closest pure cubic phase state of 92%. Generating higher fidelity cubic phase states is yet to be achieved. Generating other non-Gaussian states, such as Cat states [16] is of great interest due to their promises of being used for fault-tolerant quantum computation [17], [18]. Due to the universal control of a bosonic mode, one should expect that generating such states with this architecture could be possible. Cat states have been experimentally achieved with a SNAIL-resonator [19], [20], by combining the intrinsic Kerr effect of the SNAIL and two-photon driving [21]. However, the universal control in [13] was demonstrated while canceling out the intrinsic Kerr effect, which yields the question of how cat states can be generated in this regime by creating a driven Kerr effect.

Quantum optimal control has over the last few decades become an increasingly common and successful approach to manipulate quantum dynamical processes [22], [23]. This success has been led by the development of multiple optimal control algorithms, most notably the GRadient Ascent Pulse Engineering (GRAPE) [24] and Chopped RAndom Basis (CRAB) [25]–[28] algorithms. These methods are in general based on finding the controls of a system that generate a desired target quantum state by means of optimization, often by shaping external electromagnetic fields applied to the system. Due to the lack of methods to generate other non-Gaussian states in the SNAIL-resonator, the question arises if it is possible to achieve this by means of optimal control.

1.1 Aim

The primary aim of this project is to develop an effective way to simulate the time evolution of the SNAIL-resonator system described above, and subsequently find experimentally feasible methods of controlling the system to generate non-Gaussian states, such as cubic phase states and cat states.

The SNAIL consists of an array of Josephson Junctions (JJs) in parallel with one smaller JJ. By piercing the loop with a static magnetic flux, one can cancel the inherent Kerr effect of the SNAIL. This, along with universal control when coupled to a resonator, theoretically allows for generating arbitrary states within a small Kerr-free region in phase space.

For the effective simulation of the system, the aim is to construct an effective Hamiltonian that emulates the dynamics of the full Hamiltonian. By constructing an effective Hamiltonian, one can simplify the complex algebraic structure of the system while also eliminating its fast time dependence. This allows for enhanced physical insight while significantly reducing the computational cost of simulating the time evolution of the SNAIL-resonator.

For the controls of the system, the aim is to develop optimal control methods that find the optimal flux and charge pulses applied to the system to generate a target state. These optimal control methods require using an effective Hamiltonian, as the time evolution of the system must be simulated at each optimization step, resulting in the use of the full Hamiltonian being highly ineffective.

The optimal control methods will then be used with the aim of generating cubic phase states and cat states. The SNAIL-resonator has previously been used to achieve cubic phase states in experiment [13], and is comparatively easy to achieve due to the nature of the Hamiltonian. Achieving a cubic phase state by means of optimal control serves as a way of demonstrating and evaluating the performance of the optimal control methods. Achieving cat states should not be as easy as the cubic phase states, as there is no obvious way of controlling the Hamiltonian to do so. Hence, using optimal control for this would showcase that it is useful to achieve non-Gaussian states in the SNAIL-resonator for which a method of doing so was previously unknown.

1.2 Continuous Variable Quantum States

Bosons characteristically obey bosonic commutation relations $\left[\hat{a}, \hat{a}^\dagger\right] = 1$, for the creation and annihilation operators $\hat{a}^\dagger$ and $\hat{a}$. It is often useful to describe the state of a bosonic system by the Fock space, defined as the eigenspace of the number operator $\hat{a}^\dagger\hat{a}$

$$\hat{a}^\dagger\hat{a}\left|n\right\rangle = n\left|n\right\rangle, \quad n = 0, 1, 2, ... \tag{1.1}$$

The commutation relation along with (1.1) inherently gives the following relations for the creation and annihilation operators acting on the Fock space

$$\hat{a}^\dagger\left|n\right\rangle = \sqrt{n+1}\left|n+1\right\rangle, \quad \hat{a}\left|n\right\rangle = \sqrt{n}\left|n-1\right\rangle. \tag{1.2}$$

From this, one can see that

$$\left|n\right\rangle = \frac{\hat{a}^{\dagger n}}{\sqrt{n!}}\left|0\right\rangle, \tag{1.3}$$

where $\left|0\right\rangle$ is the vacuum state, $\hat{a}\left|0\right\rangle = 0$. This, along with normalisation $\langle 0|0\rangle = 1$, shows that the Fock states are orthonormal

$$\langle m|n\rangle = \frac{1}{\sqrt{m!n!}}\left\langle 0\right|\hat{a}^m\hat{a}^{\dagger n}\left|0\right\rangle = \delta_{m,n}, \tag{1.4}$$

since $\left\langle 0\right|\hat{a}^m\hat{a}^{\dagger n} = 0$ if $n > m$, $\hat{a}^m\hat{a}^{\dagger n}\left|0\right\rangle = 0$ if $m > n$, and $\hat{a}^m\hat{a}^{\dagger n}\left|0\right\rangle = \sqrt{m!n!}\left|0\right\rangle$ if $m = n$. All bosonic states can thus be described as

$$\left|\psi\right\rangle = \sum_{n=0}^{\infty} c_n\left|n\right\rangle, \quad \sum_{n=0}^{\infty}|c_n|^2 = 1, \tag{1.5}$$

where $\{c_n\}_{n=0}^{\infty}$ are complex valued probability amplitudes.

The Fock space is particularly useful to describe states that are superpositions of relatively few Fock states, e.g. $\left|\psi\right\rangle = (\left|1\right\rangle + \left|3\right\rangle)/\sqrt{2}$, as this gives concise and easy-to-work with expressions. There are, however, many cases in which the Fock space does not give nice expressions, one example being coherent states, defined as the unique eigenstates of the annihilation operator, $\hat{a}\left|\alpha\right\rangle = \alpha\left|\alpha\right\rangle, \alpha \in \mathbb{C}$. In Fock space this becomes

$$\left|\alpha\right\rangle = e^{-\frac{|\alpha|^2}{2}}\sum_{n=0}^{\infty}\frac{\alpha^n}{\sqrt{n!}}\left|n\right\rangle. \tag{1.6}$$

However, these states are much easier to comprehend in phase space.

1.2.1 Phase Space

By using (1.2), one can notice that the coherent state in (1.6) can be rewritten as

$$\left|\alpha\right\rangle = e^{-\frac{|\alpha|^2}{2}}e^{\alpha\hat{a}^\dagger}\left|0\right\rangle = e^{-\frac{|\alpha|^2}{2}}e^{\alpha\hat{a}^\dagger}e^{-\alpha^*\hat{a}}\left|0\right\rangle. \tag{1.7}$$

Using the Baker-Campbell-Hausdorff formula, this can be rewritten as a unitary operation acting on the vacuum

$$\left|\alpha\right\rangle = e^{\alpha\hat{a}^\dagger - \alpha^*\hat{a}}\left|0\right\rangle \equiv \hat{D}(\alpha)\left|0\right\rangle, \tag{1.8}$$

where $\hat{D}(\alpha) = \exp\left\{\alpha\hat{a}^\dagger - \alpha^*\hat{a}\right\}$ is called the displacement operator.

By deconstructing the annihilation and creation operators into position and conjugate momentum operators $\hat{x}$ and $\hat{p}$ obeying a canonical commutation relation $[\hat{x}, \hat{p}] = i\hbar$ as

$$\hat{x} = x_{\mathrm{zpf}}(\hat{a}^\dagger + \hat{a}), \tag{1.9}$$

$$\hat{p} = ip_{\mathrm{zpf}}(\hat{a}^\dagger - \hat{a}), \tag{1.10}$$

with $x_{zpf}p_{zpf} = \hbar/2$ and zpf standing for zero-point-fluctuations, the displacement operator can be rewritten as

$$\hat{D}(\alpha) = \exp\left\{ i \left(\frac{\mathrm{Im}\{\alpha\}}{x_{zpf}}\hat{x} - \frac{\mathrm{Re}\{\alpha\}}{p_{zpf}}\hat{p} \right) \right\}. \tag{1.11}$$

One can also notice that the expectation values of the position and momentum operators are given by

$$\langle \hat{x} \rangle_\alpha = 2\,\mathrm{Re}\{\alpha\} x_{zpf}, \tag{1.12}$$

$$\langle \hat{p} \rangle_\alpha = 2\,\mathrm{Im}\{\alpha\} p_{zpf}. \tag{1.13}$$

Hence the expected position and momentum are proportional to the real and imaginary parts of α respectively. With this remark, one can define position and momentum coordinates

$$\tilde{x} = \mathrm{Re}\{\alpha\} = \frac{\langle \hat{x} \rangle_\alpha}{2x_{zpf}}, \quad \tilde{p} = \mathrm{Im}\{\alpha\} = \frac{\langle \hat{p} \rangle_\alpha}{2p_{zpf}}. \tag{1.14}$$

Any coherent state can thus be written as

$$|\alpha\rangle = |\tilde{x} + i\tilde{p}\rangle = \exp\left\{ i \left(\tilde{p}\frac{\hat{x}}{x_{zpf}} - \tilde{x}\frac{\hat{p}}{p_{zpf}} \right) \right\} |0\rangle \,. \tag{1.15}$$

Similarly to classical particles, one sees that coherent states have a natural representation in phase space. However, in contrast to a classical particle, a coherent state can not be defined by a single point in phase space, as it is subject to the Heisenberg uncertainty principle, which in this case is

$$\sigma_x \sigma_p = x_{zpf} p_{zpf} = \frac{\hbar}{2}, \tag{1.16}$$

where $\sigma_\square = \sqrt{\langle \hat{\square}^2 \rangle - \langle \hat{\square} \rangle^2}$. Notice that the inequality is exact for coherent states. However, for arbitrary states $\sigma_x\sigma_p \geq \hbar/2$. This creates a desire to represent states by a joint probability distribution in phase space. That is however not possible due to $\hat{x}$ and $\hat{p}$ not commuting [29]. Instead one can use the Wigner distribution for a pure state

$$W(\tilde{x}, \tilde{p}) = \frac{1}{2\pi\hbar} \int_{-\infty}^{\infty} \psi^*(\tilde{x} + s/2)\psi(\tilde{x} - s/2) e^{i\tilde{p}s/\hbar} ds, \tag{1.17}$$

where $\psi(\tilde{x}) = \langle \tilde{x} | \psi \rangle$, which is a quasiprobability distribution as it is not positive for arbitrary ψ. Notably, integration over momentum gives

$$\int_{-\infty}^{\infty} W(\tilde{x}, \tilde{p}) d\tilde{p} = |\psi(\tilde{x})|^2, \tag{1.18}$$

whereas Fourier transforming the distribution and integrating over position gives a corresponding expression in the momentum basis. In Fig. 1.1 the Wigner distributions for a coherent state with $\alpha = 1 - 0.8i$ and a Fock state with $n = 3$ are shown for example. Notice that the Wigner distribution is negative for the Fock state in some parts of phase space.

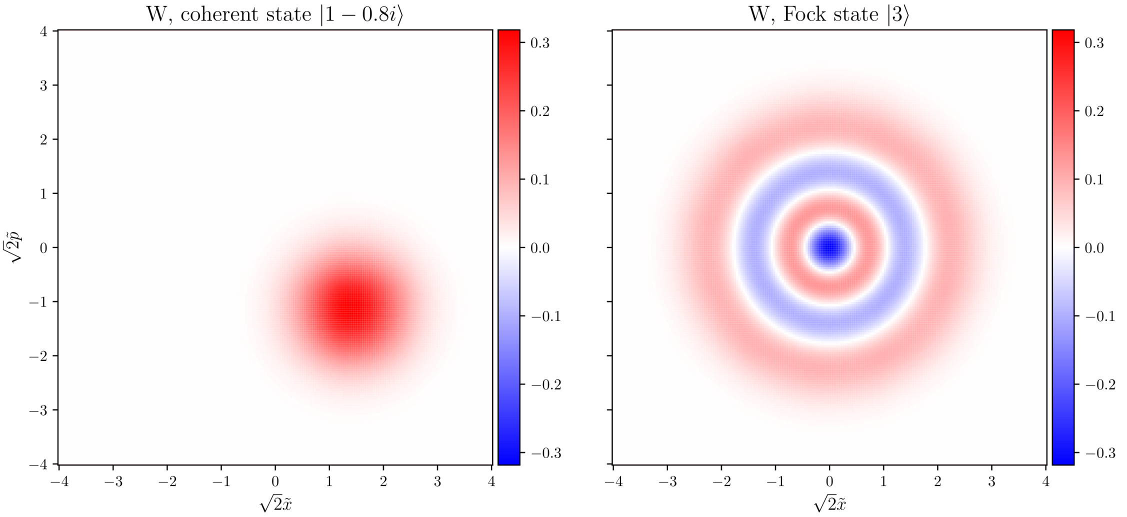

Figure 1.1: Wigner distributions for the coherent state $|1 - 0.8i\rangle$ and the Fock state $|3\rangle$.

1.2.2 Squeezed States

Another important kind of state is the squeezed coherent state. Whereas for normal coherent states, the uncertainty is given by $\sigma_x = x_{zpf}, \sigma_p = p_{zpf}$, it is possible to squeeze the state so that it is more uncertain in either position or momentum and less in the other. A squeezed coherent state $|\zeta, \alpha\rangle$ is defined by the squeezing operator $\hat{S}(\zeta)$

$$|\zeta, \alpha\rangle \equiv \hat{S}(\zeta) |\alpha\rangle \equiv \exp\left\{\frac{1}{2}\left(\zeta^* \hat{a}^2 - \zeta \hat{a}^{\dagger 2}\right)\right\} |\alpha\rangle , \tag{1.19}$$

for $\zeta \in \mathbb{C}$. Notice that $\hat{S}$ is unitary, $\hat{S}(\zeta)\hat{S}(\zeta)^\dagger = \hat{S}(\zeta)\hat{S}(-\zeta) = 1$. To explicitly see how the uncertainty changes with the squeezing parameter ζ, one can look at the standard deviation of the position and momentum σ_x, σ_p. To do this, it is first useful to calculate the transformations

$$\hat{S}(-\zeta)\hat{a}\hat{S}(\zeta) = \hat{a} \cosh r - \hat{a}^\dagger e^{i\theta} \sinh r, \tag{1.20a}$$

$$\hat{S}(-\zeta)\hat{a}^\dagger\hat{S}(\zeta) = \hat{a}^\dagger \cosh r - \hat{a} e^{i\theta} \sinh r, \tag{1.20b}$$

where $\zeta = re^{i\theta}$. This gives the following composite transformations

$$\hat{S}(-\zeta)(\hat{a}^\dagger + \hat{a})\hat{S}(\zeta) = (\hat{a}^\dagger + \hat{a})(\cosh r - e^{i\theta} \sinh r) \tag{1.21a}$$

$$\hat{S}(-\zeta)(\hat{a}^\dagger - \hat{a})\hat{S}(\zeta) = (\hat{a}^\dagger - \hat{a})(\cosh r + e^{i\theta} \sinh r). \tag{1.21b}$$

Using this along with the unitarity of the squeezing operator one can calculate the standard deviation of position

$$
\begin{aligned}
\sigma_x &= x_{zpf}\sqrt{\langle\alpha|\,\hat{S}(-\zeta)(\hat{a}^\dagger+\hat{a})^2\hat{S}(\zeta)\,|\alpha\rangle - \langle\alpha|\,\hat{S}(-\zeta)(\hat{a}^\dagger+\hat{a})\hat{S}(\zeta)\,|\alpha\rangle^2} \\
&= x_{zpf}(\cosh r - e^{i\theta}\sinh r)\sqrt{(\alpha+\alpha^*)^2 + 1 - (\alpha+\alpha^*)^2} \\
&= x_{zpf}(\cosh r - e^{i\theta}\sinh r).
\end{aligned} \tag{1.22}
$$

Similarly, one finds the standard deviation of momentum

$$
\sigma_p = p_{zpf}(\cosh r + e^{i\theta}\sinh r). \tag{1.23}
$$

Assuming that the squeezing parameter is real, i.e. $\theta = 0$, the uncertainty relations become

$$
\sigma_x = x_{zpf}e^{-r}, \quad \sigma_p = p_{zpf}e^{r}. \tag{1.24}
$$

From this, it is clear that a positive squeezing parameter exponentially decreases the uncertainty in position while increasing it in momentum, and vice versa.
Apart from the states mentioned above, three more states will be explicitly considered in this work, namely trisqueezed states, cubic phase states, and cat states. Trisqueezed states $|\tau\rangle\,, \tau \in \mathbb{C}$ are defined as

$$
|\tau\rangle \equiv \hat{T}_s(\tau)\,|0\rangle \equiv \exp\Big\{\tau\hat{a}^{\dagger 3} - \tau^*\hat{a}^3\Big\}\,|0\rangle\,. \tag{1.25}
$$

Cubic phase states $|\kappa,\zeta\rangle\,, \kappa \in \mathbb{R}$ are defined as

$$
|\kappa,\zeta\rangle \equiv \hat{C}(\kappa)\hat{S}(\zeta)\,|0\rangle\,, \quad \hat{C}(\kappa) \equiv \exp\left\{i\kappa\left(\frac{\hat{a}^\dagger+\hat{a}}{\sqrt{2}}\right)^3\right\}. \tag{1.26}
$$

Lastly, cat states are usually defined as the equal superposition of opposite phase coherent states. In this work, the cat states considered will be of the form

$$
\mathcal{N}(|\alpha\rangle + |{-\alpha}\rangle), \quad \alpha \in \mathbb{C}, \tag{1.27}
$$

with a normalization constant $\mathcal{N}$. From (1.6) one can easily find that

$$
\mathcal{N} = \frac{1}{\sqrt{2(1+e^{-2|\alpha|^2})}}. \tag{1.28}
$$

The Wigner functions of squeezed, trisqueezed, cubic phase, and cat states are shown in Figure 1.2.

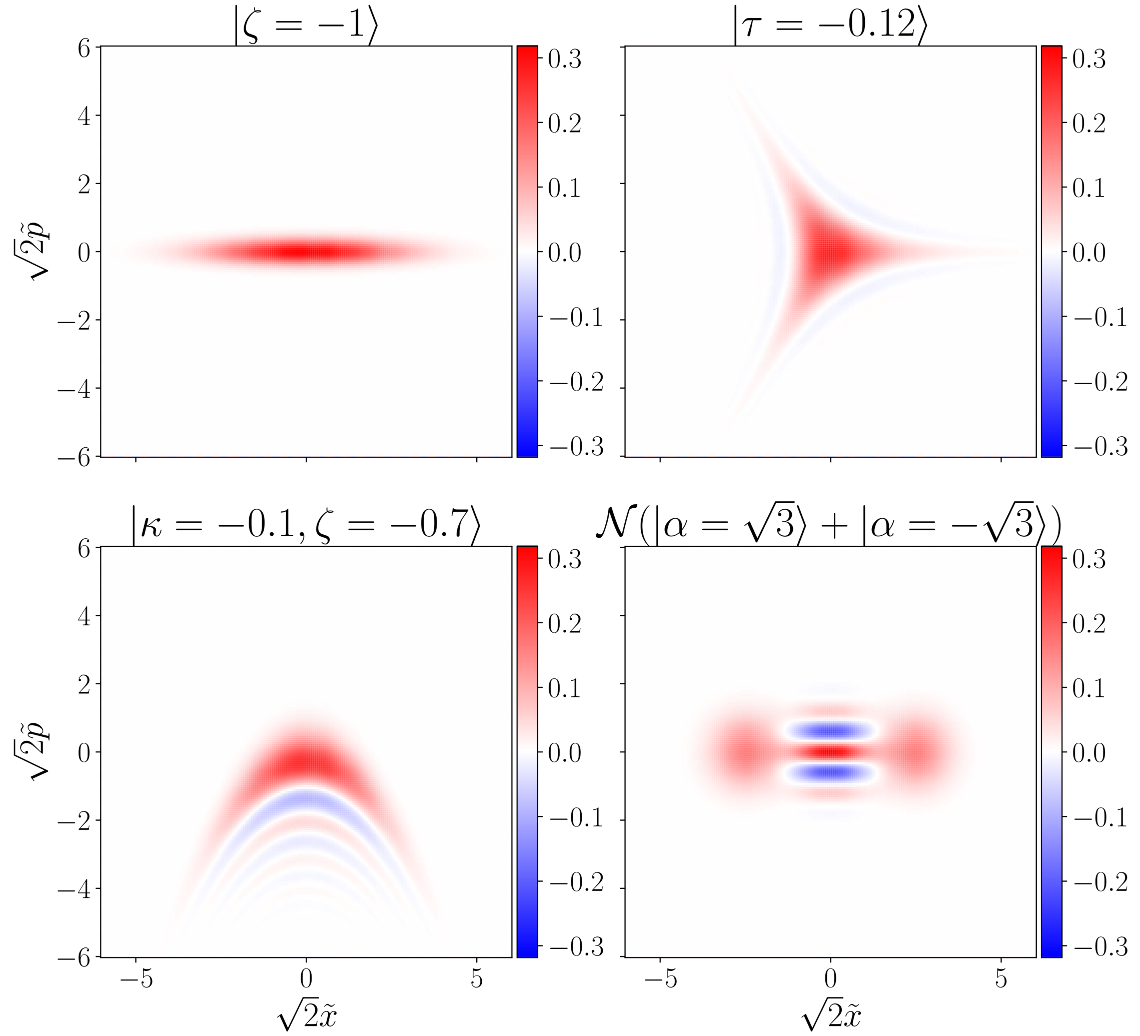

Figure 1.2: Wigner functions of squeezed (top left), trisqueezed (top right), cubic phase (bottom left) and cat (bottom right) states.

2

Theory

This chapter aims to give the theoretical background for this thesis to an extent which is necessary to understand the following chapters. The reader is assumed to have a basic understanding of quantum mechanics and undergraduate-level mathematics.
First, the formalism for deriving quantum Hamiltonians for superconducting circuits is described in Section 2.1 and methods for deriving effective Hamiltonians in Section 2.2. Lastly, the system used in this work is described in Section 2.3.

2.1 Circuit Quantum Electrodynamics

Circuit Quantum Electrodynamics (cQED) is a framework developed to quantize the electromagnetic field of superconducting circuits in the microwave frequency domain [30]. This allows for studying the non-linear quantum effects of such circuits. In the following, cQED is briefly explained to the extent necessary to understand the SNAIL-resonator circuit considered in this work. For more detail, see e.g. [31].

2.1.1 Circuit Elements

With the goal of deriving a Hamiltonian for a superconducting circuit, it is necessary to describe the energy of each circuit element, which is given by

$$E(t) = \int_{-\infty}^{t} V(t')I(t')dt', \tag{2.1}$$

with V and I being the voltage and current of the element respectively. In order to define a Lagrangian for the circuit, it is necessary to express these energies in a generalized circuit coordinate, here chosen to be the magnetic flux

$$\Phi(t) = \int_{-\infty}^{t} V(t')dt'. \tag{2.2}$$

Note that circuits with multiple nodes must be described with the same number of separate coordinates, i.e. a circuit with N nodes can be described by flux coordinates $\Phi_1, ..., \Phi_N$.
Beginning with a capacitance, its voltage is given by $V = Q/C$, which can be rewritten as $I = C\dot{V}$. Hence its energy is given by

$$E_C(t) = C\int_{-\infty}^{t} V(t')\dot{V}(t')dt' = \frac{CV(t)^2}{2} = \frac{C\dot{\Phi}(t)^2}{2}. \tag{2.3}$$

For an inductor, the flux-current relation is given by $\Phi = LI$. This gives the energy

$$E_L(t) = \frac{1}{L}\int_{-\infty}^{t} \dot{\Phi}(t')\Phi(t')dt' = \frac{\Phi(t)^2}{2L}. \tag{2.4}$$

Then, there is the Josephson Junction (JJ), which obeys the Josephson relations

$$I = I_C \sin\varphi, \quad V = \frac{\Phi_0}{2\pi}\dot{\varphi}, \tag{2.5}$$

with I_C being the critical current of the junction, $\varphi = 2\pi\Phi/\Phi_0$ being the reduced flux and $\Phi_0 = h/2e$ being the magnetic flux quantum. The energy is given by

$$E_{JJ}(t) = \frac{I_C\Phi_0}{2\pi}\int_{-\infty}^{t} \dot{\varphi}(t')\sin\varphi(t')dt' = E_J(1-\cos\varphi(t)), \tag{2.6}$$

where $E_J = I_C\Phi_0/2\pi$ is the junction-specific Josephson energy. Note that if one neglects the constant terms and assumes the reduced flux is small, $|\varphi| \ll 1$,

$$E_{JJ}(t) = \frac{E_J}{2}\varphi(t)^2 + \mathcal{O}(\varphi^4), \tag{2.7}$$

so the JJ acts approximately as a linear inductor with $L_J = \frac{\Phi_0^2}{4\pi^2 E_J}$. For larger amplitudes of the reduced flux, however, the JJ introduces non-linearities.

2.1.2 Quantization

The quantization of superconducting circuits can be performed by using the Lagrange-Hamilton formalism to derive a classical Hamiltonian, followed by promoting the classical coordinates to quantum operators. Explicitly, one first defines the Lagrangian as

$$\mathcal{L} = \mathcal{T} - \mathcal{U}, \tag{2.8}$$

with $\mathcal{T}$ and $\mathcal{U}$ being the kinetic and potential energy respectively. With magnetic flux Φ as a generalized coordinate, the kinetic energy is then related to the capacitive energies depending on $\dot{\Phi}$ and the potential energy to the inductive energies depending on Φ. The Lagrangian is then related to the classical Hamiltonian via a Legendre transformation. For this, one first defines the conjugate momentum as

$$Q = \frac{\partial\mathcal{L}}{\partial\dot{\Phi}}. \tag{2.9}$$

Note that if the only kinetic energy in the circuit is a simple capacitor, the conjugate momentum is equal to the charge of the capacitor. The Hamiltonian is subsequently given by

$$H = Q\dot{\Phi} - \mathcal{L}, \tag{2.10}$$

or for a circuit of N nodes

$$H = \sum_{i=1}^{N} Q_i\dot{\Phi}_i - \mathcal{L}, \quad Q_i = \frac{\partial\mathcal{L}}{\partial\dot{\Phi}_i}. \tag{2.11}$$

This Hamiltonian is still classical, with the flux and charge coordinates Φ and Q fulfilling the Poisson bracket

$$\{\Phi, Q\} = 1. \tag{2.12}$$

To arrive at a quantum Hamiltonian, one must promote the coordinates to quantum operators fulfilling the canonical commutation relations

$$\left[\hat{\Phi}, \hat{Q}\right] = i\hbar. \tag{2.13}$$

It is often convenient to instead use the reduced flux $\hat{\varphi}$ and reduced charge $\hat{n} = \hat{Q}/2e$,which then fulfil $[\hat{\varphi}, \hat{n}] = i$. The reduced flux is also referred to as the superconducting phase, and the reduced charge as the number of excess Cooper pairs.

2.1.3 Second Quantization

Dealing with linear and non-linear oscillators can often be made easier by rewriting the Hamiltonian to a second quantization form. Let the Hamiltonian for some linear or non-linear oscillator circuit be given by

$$\hat{H} = E_1\hat{n}^2 + E_2\hat{\varphi}^2 + (\text{N.L.}), \tag{2.14}$$

where E_1, E_2 are some energy constants and (N.L) are all the non-linear terms. One can then define ladder (elimination and creation) operators $\hat{a}$ and $\hat{a}^\dagger$ fulfilling the bosonic commutation relation $\left[\hat{a}, \hat{a}^\dagger\right] = 1$, such that

$$\hat{\varphi} = \varphi_{\text{zpf}}(\hat{a}^\dagger + \hat{a}), \tag{2.15}$$

$$\hat{n} = in_{\text{zpf}}(\hat{a}^\dagger - \hat{a}), \tag{2.16}$$

with $\varphi_{\text{zpf}} = (E_1/4E_2)^{1/4}$, $n_{\text{zpf}} = (E_2/4E_1)^{1/4}$ being the zero-point-fluctuations of the flux and charge. Hence, the Hamiltonian can be rewritten as

$$\hat{H} = \omega_r(\hat{a}^\dagger\hat{a} + 1/2) + (\text{N.L.}), \tag{2.17}$$

with $\omega_r = 2\sqrt{E_1E_2}$ being the oscillator frequency. Note that the eigenspace of $\hat{a}^\dagger\hat{a}$ is the Fock space, i.e. $\hat{a}^\dagger\hat{a}\left|n\right\rangle = n\left|n\right\rangle$, $n = 0, 1, 2, ...$

2.2 Effective Hamiltonian Theory

Driven bosonic systems inherently come with an infinite dimensional Hilbert system, and some time dependence for the system Hamiltonian induced by the driving. This means that the dynamics of the system are both difficult to simulate and to understand in general simply by examining the full Hamiltonian. A common way to deal with this is to define an effective Hamiltonian, which emulates the dynamics of the original Hamiltonian while operating on a reduced Hilbert space and eliminating or simplifying the time dependence.

For this work, the system will be weakly driven, so one can safely assume that the amplitudes of higher-level Fock states are quickly decreasing. The Hilbert space can hence be reduced simply by truncating it at some dimension of Fock space, for which the dynamics left out by excluding the remaining dimensions are negligible. Determining this dimension can be done by simulating the time evolution of the system for increasing truncation levels until it converges. The method for doing so in this work is further explained in Chapter 3.

The driving of the system in this work is limited to harmonic drives with slowly varying pulse envelopes, which induces quickly oscillating terms in the driving Hamiltonian. Below, the theoretical frameworks used to derive an effective Hamiltonian which eliminates the quickly oscillating driving terms while keeping the slow time-dependence of the pulse envelopes are described.

2.2.1 The Rotating Frame

The Hamiltonian of a quantum system can be divided as

$$\hat{H}(t) = \hat{H}_0 + \hat{V}(t), \tag{2.18}$$

where $\hat{H}_0$ contains some rather trivial rotational dynamics of the system, and $\hat{V}(t)$ contains the dynamics that one is interested in studying. In this case, one can move into a rotating frame of reference of the system which cancels out $\hat{H}_0$, by performing a so-called rotating frame transformation. This is a special case of a unitary transformation, determined by $\hat{U}(t)$ such that $\hat{U}(t)\hat{U}^\dagger(t) = 1$.

Consider $|\psi(t)\rangle$ to be the state of the system in the original lab frame, and $|\phi(t)\rangle = \hat{U}\,|\psi(t)\rangle$ the state in the transformed frame. By using the Schrödinger equation, the product rule of derivatives and the unitarity of $\hat{U}(t)$, it follows that

$$i\partial_t\,|\phi(t)\rangle = (\hat{U}(t)\hat{H}(t)\hat{U}(t)^\dagger + i\partial_t(\hat{U}(t))\hat{U}(t)^\dagger)\,|\phi(t)\rangle\,. \tag{2.19}$$

So the transformed state obeys the Schrödinger equation for a modified Hamiltonian

$$\hat{H}_I(t) = \hat{U}(t)\hat{H}(t)\hat{U}(t)^\dagger + i\partial_t(\hat{U}(t))\hat{U}(t)^\dagger. \tag{2.20}$$

Now, considering the Hamiltonian in (2.18), and letting $\hat{U}(t) = \exp\left\{i\hat{H}_0 t\right\}$, one can easily see that the Hamiltonian in the rotating frame is given by

$$\hat{H}_I(t) = \hat{U}(t)\hat{V}(t)\hat{U}(t)^\dagger = e^{i\hat{H}_0 t}\hat{V}(t)e^{-i\hat{H}_0 t}. \tag{2.21}$$

In this work, one can in general always set $\hat{H}_0 = \omega_r \hat{a}^\dagger \hat{a}$, for some frequency ω_r and bosonic ladder operators obeying $\left[\hat{a}^\dagger, \hat{a}\right] = 1$. Moreover, $\hat{V}(t)$ will in general consist of terms proportional to some product of ladder operators. It is only necessary to see how $\hat{a}$ transforms in this rotating frame, as the transformation of $\hat{a}^\dagger$ follows from the conjugate transpose. All arbitrary products of ladder operators must transform as the same product of the individually transformed ladder operators. The transformation is given by

$$\hat{a} \to e^{i\omega_r \hat{a}^\dagger \hat{a} t}\hat{a}e^{-i\omega_r \hat{a}^\dagger \hat{a} t}. \tag{2.22}$$

To rewrite this transformed operator, one can use the following special case of the Baker-Campbell-Hausdorff formula:

$$e^X Y e^{-X} = Y + [X, Y] + \frac{1}{2!}[X, [X, Y]] + \frac{1}{3!}[X, [X, [X, Y]]] + \dots\,. \tag{2.23}$$

Since $\left[\hat{a}^\dagger\hat{a},\hat{a}\right] = -\hat{a}$, the transformation becomes

$$\hat{a} \to \sum_{k=0}^{\infty} \frac{(-i\omega_r t)^k}{k!}\hat{a} = e^{-i\omega_r t}\hat{a}. \tag{2.24}$$

2.2.2 Rotating Wave Approximation

One of the most famous method of treating rapid oscillations in the Hamiltonian is known as the Rotating Wave Approximation (RWA), first observed experimentally by Rabi et al. in 1938 [32]. The RWA is here introduced for a resonantly driven Hamiltonian in the rotating frame of a resonator of some frequency ω_0, where it is assumed that the Hamiltonian can be expressed as

$$\hat{H}_I(t) = \sum_{k\in\mathbb{Z}} \hat{h}_k e^{ik\omega_0 t}. \tag{2.25}$$

The RWA in this situation boils down to approximating the effective Hamiltonian $\hat{H}_{\text{eff}} \simeq \hat{h}_0$. Note that this is equivalent to approximating $\hat{H}_{\text{eff}} \simeq \frac{1}{T}\int_0^T \hat{H}_I(t)dt$, with $T = 2\pi/\omega_0$ being the period time of the resonator, i.e. the time-average of the rotated Hamiltonian. The accuracy of this approximation relies on the rates of change for the system under each $\hat{h}_k, k \neq 0$, being small compared to ω_0 [33]–[35]. Under this condition, the system evolves under the influence of the time-independent Hamiltonian $\hat{H}_{\text{eff}}$ such that

$$|\psi(t)\rangle = e^{-i\hat{H}_{\text{eff}}(t-t_0)}|\psi_0\rangle, \tag{2.26}$$

for some initial state $|\psi_0\rangle = |\psi(t_0)\rangle$.

2.2.3 Higher-order corrections to RWA

There are many popular methods of calculating effective Hamiltonians of a higher degree of accuracy, or equivalently, higher-order corrections to the RWA. These include the Floquet-Magnus expansion [36], the van-Vleck expansion [37] and the James' effective Hamiltonian method [38]. A general, recursive formula for calculating the effective Hamiltonian of arbitrary order for a rapidly driven non-linear system (quantum or classical) was introduced in [35]. Here, this formula is applied to the Hamiltonian given by (2.25). One sees that the RWA follows the zeroth-order, and the expression for the evolved state at the first-order is relatively simple.

In the quantum mechanical case, the formula is based on transforming the density matrix $\hat{\rho}$ to $\hat{\varrho} = e^{-i\hat{S}}\hat{\rho}e^{i\hat{S}}$ for some Hermitian operator $\hat{S}$. Considering the original density matrix obeys the Liouville-von Neumann equation $\partial_t\hat{\rho} = -i\left[\hat{H},\hat{\rho}\right]$, the transformed density matrix obeys $\partial_t\hat{\varrho} = -i\left[\hat{H}_{\text{eff}},\hat{\varrho}\right]$. Here, $\hat{H}_{\text{eff}} = e^{-i\hat{S}}(\hat{H} - i\partial_t)e^{i\hat{S}}$. By imposing $\hat{H}_{\text{eff}}$ to be time-independent, and choosing $\hat{S}$ accordingly, one finds that the original density matrix at some time t is given by

$$\hat{\rho}(t) = e^{i\hat{S}(t)}e^{-i\hat{H}_{\text{eff}}(t-t_0)}e^{-i\hat{S}(t_0)}\hat{\rho}_0 e^{i\hat{S}(t_0)}e^{i\hat{H}_{\text{eff}}(t-t_0)}e^{-i\hat{S}(t)}, \tag{2.27}$$

for some initial state $\hat{\rho}_0 = \hat{\rho}(t_0)$.

Consider the rotated Hamiltonian in (2.25), and denote $\hat{H}_I = \hat{H}$ for simplicity. Take for Ansatz $\hat{S} = \sum_{k\in\mathbb{N}} \hat{S}^{(k)}$, $\hat{H}_{\text{eff}} = \sum_{k\in\mathbb{N}} \hat{H}^{(k)}_{\text{eff}}$, $\hat{S}^{(0)} = 0$ and $\hat{S}^{(k)}, \hat{H}^{(k)}_{\text{eff}} \propto 1/\omega_0^k$. By imposing $\hat{H}^{(k)}_{\text{eff}}$ to be time-independent at each step, and decomposing it as $\hat{H}^{(k)}_{\text{eff}} = \sum_{m\in\mathbb{N}} \hat{H}^{(k)}_{\text{eff},[m]}$, the following recursive formula is found [35]

$$\hat{H}^{(k)}_{\text{eff},[m]} = \begin{cases} \hat{H}, & k = m = 0 \\ \partial_t \hat{S}^{(k+1)} + \frac{1}{i}\left[\hat{S}^{(k)}, \hat{H}\right], & m = 1 \\ \sum\limits_{l=0}^{k-1} \frac{1}{im}\left[\hat{S}^{(k-l)}, \hat{H}^{(l)}_{\text{eff},[m-1]}\right], & 1 < m \leq k+1 \\ 0 & \text{otherwise,} \end{cases} \tag{2.28a}$$

$$\hat{S}^{(k+1)} = \begin{cases} -\int dt \mathbf{osc}(\hat{H}), & k = 0 \\ -\int dt \mathbf{osc}\left(\frac{1}{i}\left[\hat{S}^{k}, \hat{H}\right] + \sum\limits_{m>1}^{k+1} \sum\limits_{l=0}^{k-1} \frac{1}{im}\left[\hat{S}^{(k-l)}, \hat{H}^{(l)}_{\text{eff},[m-1]}\right] \right), & k > 0. \end{cases} \tag{2.28b}$$

Here, $\mathbf{osc}\,(f) = f - \frac{1}{T}\int_0^T dt f$. For $k = 0$, one finds that $\hat{H}^{(0)}_{\text{eff}} = \hat{H} + \partial_t \hat{S}^{(1)} + \frac{1}{i}\left[\hat{S}^{(0)}, \hat{H}\right] = \hat{H} - \mathbf{osc}(\hat{H}) = \frac{1}{T}\int_0^T dt\hat{H} = \hat{h}_0$, i.e. one recovers the RWA. At the first-order, $k = 1$, one can find that

$$\hat{H}^{(1)}_{\text{eff}} = \sum_k \frac{\left[\hat{h}_k, \hat{h}_{-k}\right]}{2k\omega_0}, \quad \hat{S}^{(1)} = \sum_k \frac{\hat{h}_k}{k\omega_0} e^{ik\omega_0 t}. \tag{2.29}$$

So for the first-order correction to the RWA, the time evolution is given by

$$\hat{\rho}(t) = e^{i\hat{S}^{(1)}(t)} e^{-i(\hat{H}^{(0)}_{\text{eff}} + \hat{H}^{(1)}_{\text{eff}})(t-t_0)} e^{-i\hat{S}^{(1)}(t_0)} \hat{\rho}_0 e^{i\hat{S}^{(1)}(t_0)} e^{i(\hat{H}^{(0)}_{\text{eff}} + \hat{H}^{(1)}_{\text{eff}})(t-t_0)} e^{-i\hat{S}^{(1)}(t)}. \tag{2.30}$$

For higher-order corrections, one can then recursively find the next order of the expansion using (2.29). Note that at order k, the effective Hamiltonian will be of order $\sim \hat{H}^{k+1}\omega_0^{-k}$. Hence, one can explicitly see that the accuracy of the approximation depends on the rate of change under $\hat{H}$ being much smaller than ω_0. The smaller this rate of change is compared to ω_0, the smaller the higher-order corrections will be.

The first-order correction in (2.29) is derived under the assumption that all $\hat{h}_k$ are time-independent. In the system studied in this work, all $\hat{h}_k$ will depend on the pulse amplitudes of the drives applied to the system. In general, these pulse amplitudes will have a time dependence that is slow compared to the resonator frequency ω_0. Formally, it is required that this time dependence is slow enough for all $\hat{h}_k$ to be considered static during one period of the resonator frequency, $2\pi/\omega_0$, for the effective Hamiltonian to be accurate.

2.3 SNAIL-Resonator Circuit

The main circuit considered in this work consists of a $\lambda/4$ coplanar waveguide resonator capacitively coupled to an input transmission line and terminated by a SNAIL [15]. This will be referred to as the SNAIL-resonator circuit. Below, the potential of a SNAIL is motivated through the framework of cQED, and thereafter the Hamiltonian of the SNAIL-resonator. Then, it is explained how driving the SNAIL-resonator by charge pumping through the transmission line and applying an external magnetic flux piercing the SNAIL gives rise to universal control of a bosonic mode, while limiting unwanted Kerr effects.

2.3.1 The SNAIL

The SNAIL (shown schematically in Fig. 2.1) is comprised of n_J Josephson junctions (JJs) in parallel with one smaller JJ. The smaller JJ is described by a parameter α, such that its Josephson energy is given by αE_J, where E_J is the Josephson energy of each of the larger JJs. If one denotes the superconducting phase over the smaller JJ by φ, the inductive energy of the SNAIL is given by

$$U(\varphi) = -E_J \left(\alpha \cos(\varphi) + n_J \cos\left(\frac{\phi_e - \varphi}{n_J} \right) \right), \tag{2.31}$$

where ϕ_e is the external flux piercing the SNAIL (from here and onwards $\hbar = 1 = 2e$ is used) [15].

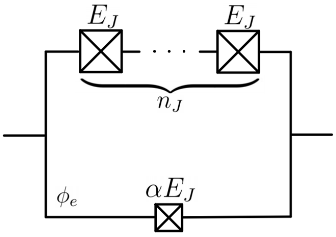

Figure 2.1: Schematic of SNAIL characterized by the Josephson energy E_J, the parameter α, and the number of JJs n_J. The loop is pierced by some magnetic flux ϕ_e.

Expanding this potential around its minimum, φ_m, determined by $\alpha \sin(\varphi_m) = \sin((\phi_e - \varphi_m)/n_J)$, gives

$$U(\varphi) = \sum_{k=2}^{\infty} \frac{1}{k!} \left. \frac{\mathrm{d}^k U}{\mathrm{d}\varphi^k} \right|_{\varphi_m} (\varphi - \varphi_m)^k, \tag{2.32}$$

where the zeroth-order term is omitted due to being constant and the first-order term is equal to zero due to the potential being minimal at φ_m.

2.3.2 The SNAIL as a Non-Linear Oscillator

Consider a capacitor with charging energy E_C in parallel with the SNAIL. The circuit Hamiltonian is then given by

$$H = \frac{E_C}{2} n^2 + U(\varphi). \tag{2.33}$$

By first performing the shift $\varphi - \varphi_m \to \varphi$, denoting

$$g_k \equiv \frac{1}{k!} \left. \frac{\mathrm{d}^k U}{\mathrm{d}\varphi^k} \right|_{\varphi_m}, \tag{2.34}$$

and then promoting n and φ to quantum mechanical operators fulfilling

$$[\hat{\varphi}, \hat{n}] = i, \tag{2.35}$$

the Hamiltonian becomes

$$\hat{H} = \frac{E_C}{2}\hat{n}^2 + g_2\hat{\varphi}^2 + \sum_{k=3}^{\infty} g_k \hat{\varphi}^k. \tag{2.36}$$

As described in subsection 2.1.3, one can define annihilation and creation operators $\hat{a}$ and $\hat{a}^\dagger$ fulfilling

$$\hat{\varphi} = \phi_{\mathrm{zpf}}(\hat{a}^\dagger + \hat{a}), \quad \hat{n} = i n_{\mathrm{zpf}}(\hat{a}^\dagger - \hat{a}), \quad \left[\hat{a}, \hat{a}^\dagger\right] = 1, \tag{2.37}$$

where

$$\phi_{\mathrm{zpf}} = \left(\frac{E_C}{8g_2}\right)^{1/4}, \quad n_{\mathrm{zpf}} = \left(\frac{g_2}{2E_C}\right)^{1/4}, \tag{2.38}$$

and

$$g_2 = \frac{E_J}{2}\left(\alpha \cos\left(\varphi_m\right) + \frac{1}{n_J}\cos\left(\frac{\phi_e - \varphi_m}{n_J}\right)\right). \tag{2.39}$$

This gives the Hamiltonian of a non-linear oscillator

$$\hat{H} = \omega_r \hat{a}^\dagger \hat{a} + \sum_{k=3}^{\infty} g_k \phi_{\mathrm{zpf}}^k (\hat{a}^\dagger + \hat{a})^k, \tag{2.40}$$

with oscillator frequency

$$\omega_r = \sqrt{2E_C g_2}. \tag{2.41}$$

2.3.3 The SNAIL-resonator Hamiltonian

A $\lambda/4$ coplanar waveguide resonator can be described by the continuous limit of a discretized series of LC-oscillators, which gives the Hamiltonian of an infinite series of harmonic oscillators

$$\hat{H} = \sum_{i=0}^{\infty} \omega_i \hat{a}_i^\dagger \hat{a}_i, \tag{2.42}$$

where the frequency of mode i is $\omega_i = (i+1)\omega_0$, with the frequency of the fundamental mode $\omega_0 = (\pi/2)(v/d)$ for wave velocity v and resonator length d [30].
Coupling this resonator to a SNAIL, essentially means that the frequency of the fundamental mode is shifted by the linear part of the SNAIL potential, while non-linearities of the SNAIL potential are introduced to the Hamiltonian. Following [13], one can model this by temporarily neglecting the non-linear terms of the SNAIL potential, resulting in a linear inductor with $L_J = 1/2g_2$ coupled to the anti-node of the discretized resonator, and then adding back the non-linearities retroactively.

Only considering the fundamental mode of the SNAIL-resonator, it is shown that the Hamiltonian is given by

$$\hat{H} = \omega_0 \hat{a}^\dagger \hat{a} + \sum_{k=3}^{\infty} g_k \hat{\varphi}^k, \quad \hat{\varphi} = \varphi_{\text{zpf}}(\hat{a}^\dagger + \hat{a}), \tag{2.43}$$

with

$$\frac{\omega_0}{\omega_\infty} = \frac{2}{\pi} \arctan\left(\frac{Z}{L_J \omega_0}\right), \tag{2.44a}$$

$$\varphi_{\text{zpf}} = \sqrt{\frac{Z}{\pi\omega_0/\omega_\infty} \frac{1+\cos(\pi\omega_0/\omega_\infty)}{1+\operatorname{sinc}(\pi\omega_0/\omega_\infty)}}, \tag{2.44b}$$

where Z is the impedance of the resonator and $\omega_\infty = (\pi/2)(v/d)$ is the fundamental frequency of the resonator in the absence of the SNAIL. Note that (2.44a) is solved numerically for ω_0.

2.3.4 The Kerr free point

From the Hamiltonian in (2.43), one can see that there exists a Kerr term

$$K^{(2)} \hat{a}^\dagger \hat{a}^\dagger \hat{a} \hat{a} = 6 g_4 \varphi_{\text{zpf}}^4 \hat{a}^\dagger \hat{a}^\dagger \hat{a} \hat{a}. \tag{2.45}$$

The external flux piercing the SNAIL has yet to be specified, and can be tuned to remove this term by solving for $g_4 = 0$, i.e.

$$\alpha \cos(\varphi_m) + \frac{1}{n_J^3} \cos\left(\frac{\phi_e^{\text{dc}} - \varphi_m}{n_J}\right) = 0, \tag{2.46}$$

for some flux bias point ϕ_e^{dc}. Thus, unwanted Kerr effects are removed.
Although illustrative, the above is a rather naive argument as g_4 does not fully describe the full Kerr effects of the system. Considering a static flux drive ϕ_e and moving to the rotating frame of the resonator, one can derive an effective Hamiltonian of the form

$$\hat{H}_{\text{eff}} = \delta \hat{a}^\dagger \hat{a} + \sum_{n\geq 2} K^{(n)} \hat{a}^{\dagger n} \hat{a}^n, \tag{2.47}$$

where δ, $K^{(n)}$ depend on ϕ_e [39]. Note that $K^{(2)} \neq 6 g_4 \varphi_{zpf}^4$ exactly, but is determined perturbatively following (2.28). For a coherent state $|\alpha\rangle$, it follows from definition that $\langle\alpha|\, \hat{a}\, |\alpha\rangle = \alpha$. Considering a small time T such that δT, $K^{(n)} T \ll 1$, the evolved state $|\tilde{\alpha}\rangle = \exp\left\{-i\hat{H}_{\text{eff}} T\right\} |\alpha\rangle$ gives

$$\langle\tilde{\alpha}|\, \hat{a}\, |\tilde{\alpha}\rangle = \langle\alpha|\, e^{i\hat{H}_{\text{eff}}T} \hat{a} e^{-i\hat{H}_{\text{eff}}T} \,|\alpha\rangle \simeq \langle\alpha|\, \hat{a}\, |\alpha\rangle + iT \langle\alpha| \left[\hat{H}_{\text{eff}}, \hat{a}\right] |\alpha\rangle . \tag{2.48}$$

In this regime of small T, it then follows that for $\alpha \in \mathbb{R}_{>0}$

$$\arg\tilde{\alpha} \simeq -\left(\delta + \sum_{n\geq 2} n K^{(n)} |\alpha|^{2(n-1)}\right) T. \tag{2.49}$$

So for small timescales, coherent states have a rotation in phase space depending on $|\alpha|^2$. The unwanted Kerr effects can thus be suppressed in a small region in phase space by tuning the static flux ϕ_e such that $\arg\tilde{\alpha} \simeq 0$ for $|\alpha| \lesssim 1$. In this region, the system will then behave as linear oscillator.

2.3.5 Driven SNAIL-resonator

So far, the SNAIL-resonator circuit has been considered to be completely static, resulting in a slightly non-linear oscillator. However, it is possible to apply time-dependent drives to the circuit by either charge pumping through the input transmission line or by adding a small time modulation to the external flux piercing the SNAIL. These drives give universal control of the fundamental mode of the SNAIL-resonator through the ability to perform rotations (which are trivial), displacements, squeezing, and trisqueezing [14].

By adding a small time modulation to the flux drive

$$\phi_e(t) = \phi_e^{\mathrm{dc}} + \phi_e^{\mathrm{ac}}(t), \quad |\phi_e^{\mathrm{ac}}(t)| \ll 1, \tag{2.50}$$

and a charge pump

$$\xi(t)(\hat{a}^\dagger + \hat{a}), \quad \xi(t) = A\cos(\omega_0 t + \gamma), \tag{2.51}$$

one can rewrite the SNAIL-resonator Hamiltonian ((2.43)) as

$$\hat{H}(t) = \omega_0 \hat{a}^\dagger \hat{a} + \xi(t)(\hat{a}^\dagger + \hat{a}) + \sum_{k=1}^{\infty}\sum_{j=1}^{\infty}(g_k^{\mathrm{dc}} + g_{k,j}^{\mathrm{ac}}\phi_e^{\mathrm{ac}}(t)^j)(\hat{a}^\dagger + \hat{a})^k, \tag{2.52}$$

with $g_1^{\mathrm{dc}} = g_2^{\mathrm{dc}} = 0$ and the remaining coefficients being given by

$$g_k^{\mathrm{dc}} = \frac{\varphi_{zpf}^k}{k!}\left(\frac{\partial^k U}{\partial \varphi^k}\right)_{\varphi_m, \phi_e^{\mathrm{dc}}}, \quad g_{k,j}^{\mathrm{ac}} = \frac{\varphi_{zpf}^k}{k!j!}\left(\frac{\partial^j}{\partial \phi_e^j}\frac{\partial^k U}{\partial \varphi^k}\right)_{\varphi_m, \phi_e^{\mathrm{dc}}}. \tag{2.53}$$

The coefficients are decreasing with k and j, and the sums can hence be truncated at some appropriate level while maintaining high accuracy to the full sums. This will be further discussed in Chapter 4.

To study the effects of these drives, it is useful to move into the rotating frame of the resonator and apply the RWA. Doing so for the charge pump term gives

$$A\cos(\omega_0 t + \gamma)(\hat{a}^\dagger + \hat{a}) \to A(e^{-i\gamma}\hat{a}^\dagger + e^{i\gamma}\hat{a}). \tag{2.54}$$

Looking only at the leading-order terms induced by the flux drive $\phi_e^{\mathrm{ac}}(t) = B\cos(n\omega_0 t + \theta)$, $n = 1, 2, 3$, the RWA gives

$$B\cos(\omega_0 t + \theta)g_{1,1}^{\mathrm{ac}}(\hat{a}^\dagger + \hat{a}) \to Bg_{1,1}^{\mathrm{ac}}(e^{-i\theta}\hat{a}^\dagger + e^{i\theta}\hat{a}), \tag{2.55a}$$

$$B\cos(2\omega_0 t + \theta)g_{2,1}^{\mathrm{ac}}(\hat{a}^\dagger + \hat{a})^2 \to Bg_{2,1}^{\mathrm{ac}}(e^{-i\theta}\hat{a}^{\dagger 2} + e^{i\theta}\hat{a}^2), \tag{2.55b}$$

$$B\cos(3\omega_0 t + \theta)g_{3,1}^{\mathrm{ac}}(\hat{a}^\dagger + \hat{a})^3 \to Bg_{3,1}^{\mathrm{ac}}(e^{-i\theta}\hat{a}^{\dagger 3} + e^{i\theta}\hat{a}^3). \tag{2.55c}$$

From this, one can see that driving the system in tones of its resonator frequency for some time T gives displacement with $\alpha = iATe^{-i\gamma}$ or $\alpha = iBTg_{1,1}^{\mathrm{ac}}e^{-i\theta}$, squeezing with $\zeta = -i2BTg_{2,1}^{\mathrm{ac}}e^{-i\theta}$, and trisqueezing with $\tau = iBTg_{3,1}^{\mathrm{ac}}e^{-i\theta}$. Furthermore, by including the second to leading-order term of the $1\omega_0$ flux drive, $3Bg_{3,1}^{\mathrm{ac}}(\hat{a}^{\dagger 2}\hat{a} + \hat{a}^\dagger + \text{h.c.})$, one can notice that applying $\xi(t) = -g_{1,1}^{\mathrm{ac}}B(t)\cos(\omega_0 t)$, and $\phi_e^{\mathrm{ac}}(t) = B(t)(\cos(\omega_0 t) + \cos 3\omega_0 t)$, the displacements cancel and generate a cubic phase gate with cubicity $\kappa = -\sqrt{2}BTg_{3,1}^{\mathrm{ac}}$.

This gives a clear intuition for how driving the system affects its fundamental mode, but is unfortunately not fully accurate. Many terms which have been neglected must also be taken into account, and higher-order corrections to the RWA also turn out to be non-negligible. This is further discussed in Chapter 4.

3

Methods

In this section, the general methods used in this work are described. First, the methods used for effectively simulating the dynamics of the SNAIL-resonator are explained in Section 3.1. However, note that the actual effective Hamiltonian of the system is found in Section 4.1. Then, the optimal control methods used are described in Section 3.2.

3.1 Effective Hamiltonian Simulation

The methods used to simulate the Hamiltonian of the SNAIL-resonator are described below. This consists of solving the Schrödinger equation (Section 3.1.1) in a properly truncated Hilbert space (Section 3.1.3) after tuning the static bias point to cancel Kerr effects (Section 3.1.2).

3.1.1 Solving the Schrödinger Equation

Simulating the dynamics of a quantum system consists of solving the Schrödinger equation

$$i\partial_t |\psi\rangle = \hat{H}(t) |\psi\rangle . \tag{3.1}$$

For a general, time-dependent Hamiltonian that does not commute with itself at all times, the solution to this is given by $|\psi(t)\rangle = \hat{U}(t, t_0) |\psi(t_0)\rangle$, where

$$\hat{U}(t, t_0) = 1 + \sum_{n=1}^{\infty} (-i)^n \int_{t_0}^{t} dt_1 \int_{t_0}^{t_1} dt_2 ... \int_{t_0}^{t_{n-1}} dt_n \hat{H}(t_1)\hat{H}(t_2)...\hat{H}(t_n), \tag{3.2}$$

for some initial time t_0 [40]. As one can see, calculating the unitary above analytically for a general Hamiltonian is incredibly difficult if not impossible, leaving a need for computationally solving the Schrödinger equation. In this work, `sesolve` from QuTiP [41] is used which integrates the Schrödinger equation for a given Hamiltonian and initial state.

In this work, the Hamiltonian to be simulated will often be an effective Hamiltonian derived according to Section 2.2. In this derivation, it is assumed that the slow time dependence of the pulses is approximately constant over the resonator period $T = 2\pi/\omega_0$ (see Section 4.1.3). Assuming that the Hamiltonian is also approximately constant over a period, solving Schrödinger equation for initial time $t = 0$ gives

$$|\psi(T)\rangle \simeq e^{-i\hat{H}(0)T} |\psi(0)\rangle , \tag{3.3}$$

and for n periods

$$|\psi(nT)\rangle \simeq \prod_{k=0}^{n-1} e^{-i\hat{H}(kT)T} |\psi(0)\rangle \,. \tag{3.4}$$

Calculating this is significantly faster than using `sesolve`, and is therefore used for all effective Hamiltonians in this work.

3.1.2 Calibrating the Kerr-free Point

In order to calibrate the optimal flux bias point to cancel Kerr effects, the rotations of coherent states under static drives are studied. As seen in the theory of Section 2.3.4, the rotation of a coherent state $|\alpha\rangle$ depends on $K^{(n)}|\alpha|^{2n}$, $n \geq 2$ on sufficiently small timescales. By tuning the flux bias point, ϕ_e^{dc}, such that coherent states with $|\alpha| \lesssim 1$ do not rotate, one should be able to find the optimal bias point.

By defining a set of coherent initial states $\{|\alpha_k\rangle\}_{k=1}^{N} = \{|0.1 + 0.05k\rangle\}_{k=1}^{N}$ and the corresponding evolved coherent states $\{|\tilde{\alpha}_k\rangle\}_{k=1}^{N} = \{\exp\!\Big(-i\hat{H}^{\mathrm{dc}}(\phi_e^{\mathrm{dc}})T\Big)\, |\alpha\rangle_k\}_{k=1}^{N}$ for a given bias point ϕ_e^{dc}, evolution time T and set size N, one can measure the Kerr effects κ as

$$\kappa(\phi_e^{\mathrm{dc}}) = \sum_k |\arg(\tilde{\alpha}_k)| = \sum_k |\arg(\langle\alpha_k|\, e^{i\hat{H}^{\mathrm{dc}}(\phi_e^{\mathrm{dc}})T} \hat{a} e^{-i\hat{H}^{\mathrm{dc}}(\phi_e^{\mathrm{dc}})T} \,|\alpha_k\rangle)|. \tag{3.5}$$

Note that the absolute values of the rotations are needed to prevent that negative and positive rotations cancel. For an ideal bias point, i.e. $K^{(n)} = 0 \quad \forall n$, one sees from (2.49) that $\kappa = \delta N T$. Since δ only redefines the resonator frequency, it is not necessary for this to equal zero. Hence, we redefine our measure of Kerr-effects as

$$\tilde{\kappa}(\phi_e^{\mathrm{dc}}) = \sum_{k\geq 2} |\arg(\tilde{\alpha}_k) - \arg(\tilde{\alpha}_1)| \simeq \sum_{k\geq 2} |\arg(\tilde{\alpha}_k) - \delta T)|, \tag{3.6}$$

meaning that the optimal bias point is given by

$$\phi_{e,opt}^{\mathrm{dc}} = \arg\min_{\phi_e^{\mathrm{dc}}} \Big(\tilde{\kappa}(\phi_e^{\mathrm{dc}})\Big)\,. \tag{3.7}$$

Since calculating $\tilde{\kappa}(\phi_e^{\mathrm{dc}})$ is computationally inexpensive, it is in general sufficient to find $\phi_{e,opt}^{\mathrm{dc}}$ by sweeping a range of reasonable bias points.

As mentioned in Section 2.3.4, it is necessary that δT, $K^{(n)}T \ll 1$ in order to study the Kerr effects in terms of rotations of coherent states. One can thus set T to be the period time of the resonator ($T = \frac{2\pi}{\omega_0}$) since this ensures that δT, $K^{(n)}T \propto \frac{g_k^{\mathrm{dc}}}{\omega_0}$ for $k = 3, 4, ...$ (only considering the leading order in ω_0^{-1}) which is guaranteed to be small for normal circuit parameters.

A reasonable choice of the set size is $N \leq 18$, since this means $\alpha_N \leq 1$. However, choosing $N > 18$ allows for generating a larger Kerr free zone, since then $\alpha_N > 1$. Hence, a simple strategy for maximizing the size of the Kerr free zone is to increase N in steps while ensuring that $\frac{1}{N-1}\min(\tilde{\kappa}(\phi_e^{\mathrm{dc}}))$ does not increase too much.

3.1.3 Truncating the Hilbert Space

To accurately simulate the dynamics of the system, its Hilbert space must be truncated at some appropriate dimension N_{dim}. To find this truncation level, one can simulate the dynamics of the system for $n = 1, 2, ...$ dimensions and define the vector representations of the simulated states for n-dimensional Fock space as v_n. By writing the d-dimensional scalar product of two vectors $u_n, v_{n'}$ of dimensions $n, n' \geq d$ as $\langle u_n, v_{n'} \rangle_d$, one can define the measures

$$\mathcal{F}(n) = |\langle v_n^\dagger, v_{n+1} \rangle_n|^2, \quad \mathcal{F}_N(n) = |\langle v_n^\dagger, v_N \rangle_n|^2. \tag{3.8}$$

By the d-dimensional scalar product, it is meant that the standard scalar product is calculated using only the first d Fock levels. Note that here v_{n+1} and v_N are first normalized to n dimensions. Using these measures, the aim is to determine when the simulation converges as $\mathcal{F}(n)$ and $\mathcal{F}_N(n)$ approach 1 for some large N.

3.2 Optimal Control Methods

With the aim of generating non-Gaussian target states with the SNAIL-resonator by means of optimal control, the method of doing so is described below.

3.2.1 Defining the Optimization Problem

The optimization problem to be solved is to find some controls for the SNAIL-resonator that evolves a given initial state to some desired target state. The controls, in this case, meaning a set of flux and charge pulses applied to the system over a set duration. Defining the realized state by some specific controls as $|\psi_c\rangle$ and the target state as $|\psi_{target}\rangle$, the aim is to maximize the overlap $|\langle \psi_{target}|\psi_c\rangle|^2$.

To initialize the controls (i.e. pulses) as optimization variables, it is first necessary to determine the total duration of the pulses T_{dur}. Then, the duration is split into a number of segments, N_s, and corresponding segment durations $\{T_i\}_{i=1}^{N_s}$ such that $\sum_i T_i = T_{dur}$. A pulse $f(t)$ can thus be defined by its type (charge or flux), its frequency $n\omega_0$, a phase θ and a set of amplitudes $\{A_i\}_{i=1}^{N_s}$. Without filtering the signal and applying an envelope function (which will be done below), the pulse is then given by

$$f(t) = A(t)\cos(n\omega_0 t + \theta), \quad A(t) = A_k \text{ for } k = \max\{k' : \sum_{i=1}^{k'-1} T_i < t\}. \tag{3.9}$$

The set of amplitudes can then be used as optimization variables. Moreover, the phase can either be fixed or also used as an optimization variable.

Since the pulse amplitude above is discrete, one can enforce it to be continuous by convolving it with some filtering function (i.e. a convolution kernel). In this work, a sinc-function is used, such that

$$f_{filtered}(t) = \sum_{i=1}^{N_s} A_i \int_{\tau_i}^{\tau_{i+1}} \frac{\sin(\omega_c(t-\tau))}{\pi(t-\tau)} d\tau, \quad \tau_1 = 0, \, \tau_{i>1} = \sum_{k=1}^{i-1} T_k. \tag{3.10}$$

The frequency ω_c is referred to as the cutoff-frequency. In the frequency domain $\sin(\omega_c t)/\pi t$ is constant in the range $[-\omega_c, \omega_c]$, such that all frequencies outside of this range are filtered. Effectively, this limits the rate of change for the pulse amplitude. Lastly, it is also necessary that the start and end of the pulses are tied to zero, $f(0) = f(T_{dur}) \simeq 0$. This is done by multiplying the pulse by a Gaussian envelope

$$\Omega(t) = \begin{cases} \exp\left(-\frac{(t-t_1)^2}{2\sigma^2}\right), & t < t_1 \\ 1, & t_1 \leq t \leq t_2 \\ \exp\left(-\frac{(t-t_2)^2}{2\sigma^2}\right), & t > t_2, \end{cases} \tag{3.11}$$

where $t_1 = t_0 - t_{flat}/2$, $t_2 = t_0 + t_{flat}/2$, for center-time $t_0 = T_{dur}/2$, flat duration t_{flat} and width σ. The final pulse is then given by

$$f(t) = f_{filtered}(t) \cdot \Omega(t). \tag{3.12}$$

For a set of flux pulses $\{\phi_i(t)\}_i$ and charge pulses $\{\xi_i(t)\}_i$, the Hamiltonian is defined as in (2.52) with $\phi_e^{\mathrm{ac}}(t) = \sum_i \phi_i(t)$ and $\xi(t) = \sum_i \xi_i(t)$. Given some initial state, the dynamics of the system are then simulated by means of an effective Hamiltonian, resulting in a state $|\psi(\phi_i, \xi_i)\rangle$. The amplitudes (and possibly phases) of the pulses can then be optimized to minimize the cost function

$$C(\phi_i, \xi_i) = 1 - |\langle\psi_{target}|\psi(\phi_i, \xi_i)\rangle|^2. \tag{3.13}$$

3.2.2 Optimization

The optimization of the problem described above is performed by using the Python package Boulder Opal [42] from Q-CTRL. This is done by performing closed loop optimization with the Covariance Matrix Adaption Evolution Strategy (CMA-ES) algorithm. The cost function for some specific controls is written entirely using QuTiP, where the evolution from some initial state is simulated according to (3.4) and the cost is calculated according to (3.13). Furthermore, the optimizer requires setting bounds on the optimization variables, a target cost, a maximum number of iterations and some initial controls. The bounds are determined according to the relations found between the accuracy of the Hamiltonian and the pulse amplitudes found in Section 4.1.4. The initial controls are then chosen randomly within the bounds, and the target cost and maximum number of iterations are chosen to give a low cost without being too computationally expensive.

For an optimization problem with n optimization variables, the CMA-ES algorithm works by drawing λ samples from a n-dimensional multivariate normal distribution. The cost function is then evaluated for each sample, and this information is used to update the normal distribution from which the next generation of samples will be drawn. In general, this is done by generating a new mean vector and covariance matrix from weighted functions of the $\mu \leq \lambda$ best samples, based on maximizing the likelihood of selecting those μ samples in the next generation. In order to increase the performance and speed of the algorithm, it is also typical to include two evolution paths in order to generate the new covariance matrix as well as controlling the overall step-size of the algorithm. Notably, this algorithm does not require the calculation of a gradient of the cost function, and is effective for non-linear and non-convex optimization problems. [43]

4

Results

The results of this thesis are divided into two parts. First, effective Hamiltonian modeling is covered in Section 4.1, where an effective Hamiltonian of the SNAIL-resonator is derived and its accuracy to the full Hamiltonian is analyzed. Then, the effective Hamiltonian is used to generate cubic phase and cat states by means of optimal control in Section 4.2.

4.1 Effective Hamiltonian Modelling

Below, an effective Hamiltonian for the SNAIL-resonator is derived from its full Hamiltonian given by (2.52). This is done by truncating the series to finite sums (Section 4.1.1), and deriving effective Hamiltonian and micromotion operators to reach a finite accuracy to the full Hamiltonian (Section 4.1.2). Subsequently, the relation between the rate of change of pulse amplitudes and the accuracy of the effective Hamiltonian is studied (Section 4.1.3). Lastly, the accuracy of the effective Hamiltonian is studied by simulation of the time evolution of the system (Section 4.1.4).

Throughout this section, the flux bias point is set to $\phi_e^{\mathrm{dc}} = 0.3912 \times 2\pi$, which approximately cancels Kerr effects, and the following circuit parameters are used:

Parameter	Symbol	Value
SNAIL-asymmetry	α	0.097
SNAIL-resonator impedance	Z	$57.94\,\Omega = 0.05641 R_q$
Number of JJs in SNAIL leg	n_J	3
Free resonator frequency	$\omega_\infty/2\pi$	8.99 GHz
Large JJ energy	E_J	245 GHz

Table 4.1: Circuit parameters used in all of the following simulations. The same circuit parameters are given in Eriksson et al. [13]. Since $\hbar = 2e = 1$ is used, the SNAIL-resonator impedance is also given in units of $R_q = \hbar/(2e)^2 \simeq 1027\,\Omega$.

4.1.1 Truncating the Hamiltonian to Finite Sums

The full Hamiltonian for a static flux drive ($\phi_e^{\mathrm{ac}}(t) = \xi(t) = 0$) is given by

$$\hat{H}^{\mathrm{dc}} = \omega_0 \hat{a}^\dagger \hat{a} + \sum_{k=3}^{\infty} g_k^{\mathrm{dc}} (\hat{a}^\dagger + \hat{a})^k, \quad g_k^{\mathrm{dc}} = \frac{\varphi_{zpf}^k}{k!} \left(\frac{\partial^k U}{\partial \varphi^k} \right)_{\varphi_m, \phi_e^{\mathrm{dc}}}. \tag{4.1}$$

For the effective Hamiltonian, one needs to first truncate the sum to some $k = N$. An appropriate choice for this is given by the smallest N such that $g^{\mathrm{dc}}_{N+1}/g^{\mathrm{dc}}_4 < 10^{-3}$. As g^{dc}_k decreases with k, this ensures that the neglected terms are much smaller than the leading-order contribution to the Kerr effect. By calculating g^{dc}_k for $k = 4, 5, 6, ...$, one will see that $g^{\mathrm{dc}}_{N+1}/g^{\mathrm{dc}}_4 < 10^{-3}$ for $N \geq 6$. Hence, we choose the truncation such that the static Hamiltonian is given by

$$\hat{H}^{\mathrm{dc}}_{N=6} = \omega_0 \hat{a}^\dagger \hat{a} + \sum_{k=3}^{6} g^{\mathrm{dc}}_k (\hat{a}^\dagger + \hat{a})^k. \tag{4.2}$$

One can also note that this truncation is also appropriate when applying a time dependent drive, as the leading-order contributions of these drives are given by $g^{\mathrm{ac}}_{1,j}$ and $g^{\mathrm{ac}}_{7,j}/g^{\mathrm{ac}}_{1,j} \sim \varphi^6_{zpf} \sim 10^{-6}$. By truncating the Hamiltonian at $N = 6$ also when applying a time-dependent flux drive, it reads as

$$\hat{H}_{N=6}(t) = \omega_0 \hat{a}^\dagger \hat{a} + \sum_{k=1}^{6} \sum_{j=1}^{\infty} (g^{\mathrm{dc}}_k + g^{\mathrm{ac}}_{k,j} \phi^{\mathrm{ac}}_e(t)^j)(\hat{a}^\dagger + \hat{a})^k, \tag{4.3}$$

with $g^{\mathrm{dc}}_1 = g^{\mathrm{dc}}_2 = 0$ and the remaining coefficients g^{dc}_k and $g^{\mathrm{ac}}_{k,j}$ given by (2.53). Naturally, the very next step in deriving an effective Hamiltonian is to truncate the second sum to some $j = M$. By considering a similar condition as before, namely $g^{\mathrm{ac}}_{k,M+1}|\phi^{\mathrm{ac}}_e(t)^M|/g^{\mathrm{ac}}_{k,1} < 10^{-3}\ \forall k$, one can choose $M = 2$ if $|\phi^{\mathrm{ac}}_e(t)| \leq 0.03697 \times 2\pi$ at all times t. By also considering a time-dependent charge drive, the Hamiltonian is given by

$$\hat{H}_{M=2}(t) = \omega_0 \hat{a}^\dagger \hat{a} + \xi(t)(\hat{a}^\dagger + \hat{a}) + \sum_{k=1}^{6} (g^{\mathrm{dc}}_k + g^{\mathrm{ac}}_{k,1} \phi^{\mathrm{ac}}_e(t) + g^{\mathrm{ac}}_{k,2} \phi^{\mathrm{ac}}_e(t)^2)(\hat{a}^\dagger + \hat{a})^k, \tag{4.4}$$

where

$$\begin{aligned} g^{\mathrm{dc}}_k &= \frac{\varphi^k_{zpf}}{k!} \left(\frac{\partial^k U}{\partial \varphi^k} \right)_{\varphi_m, \phi^{\mathrm{dc}}_e}, \\ g^{\mathrm{ac}}_{k,1} &= \frac{\varphi^k_{zpf}}{k!} \left(\frac{\partial}{\partial \phi_e} \frac{\partial^k U}{\partial \varphi^k} \right)_{\varphi_m, \phi^{\mathrm{dc}}_e}, \\ g^{\mathrm{ac}}_{k,2} &= \frac{1}{2} \frac{\varphi^k_{zpf}}{k!} \left(\frac{\partial^2}{\partial \phi^2_e} \frac{\partial^k U}{\partial \varphi^k} \right)_{\varphi_m, \phi^{\mathrm{dc}}_e}, \end{aligned} \tag{4.5}$$

and $g^{\mathrm{dc}}_1 = g^{\mathrm{dc}}_2 = 0$.

4.1.2 The Resonantly Driven Hamiltonian

As discussed in Section 2.3.5, universal control of the fundamental mode of the SNAIL-resonator is obtained from applying flux pulses of frequencies $\omega_0, 2\omega_0, 3\omega_0$ and charge pulses of frequency ω_0. One can thus constrain $\xi(t)$ and $\phi^{\mathrm{ac}}_e(t)$ to be resonant drives of the form

$$\xi(t) = \sum_m v_m(t) \cos(\omega_0 t + \gamma_m), \tag{4.6a}$$

$$\phi^{\mathrm{ac}}_e(t) = \sum_{n=1}^{3} \sum_m u_{n,m}(t) \cos(n\omega_0 t + \theta_{n,m}), \tag{4.6b}$$

where $v_m(t)$ and $u_{n,m}(t)$ are slowly varying pulse amplitudes and m is an index over different pulses of the same frequency. What is meant by slowly varying will be defined in Section 4.1.3. Furthermore, moving into the rotating frame of frequency ω_0 gives the rotated Hamiltonian

$$\begin{aligned}\hat{H}_I(t) &= \xi(t)(\hat{a}^\dagger e^{i\omega_0 t} + \hat{a}e^{-i\omega_0 t}) + \\ &+ \sum_{k=1}^{6}(g_k^{\text{dc}} + g_{k,1}^{\text{ac}}\phi_e^{\text{ac}}(t) + g_{k,2}^{\text{ac}}\phi_e^{\text{ac}}(t)^2)(\hat{a}^\dagger e^{i\omega_0 t} + \hat{a}e^{-i\omega_0 t})^k.\end{aligned} \tag{4.7}$$

By combining (4.6) and (4.7), it is evident that the Hamiltonian can be rewritten to the form

$$\hat{H}_I(t) = \sum_{m=-12}^{12} \hat{h}_m(t)e^{im\omega_0 t}, \tag{4.8}$$

where $\hat{h}_m(t)$ are slowly varying in time along with the drive amplitudes. To avoid confusion, note that this m is not related to the sum over pulses in (4.6). The rotating terms $\hat{h}_m(t)$ all have relatively complicated forms, and are hence given in Appendix A. An effective Hamiltonian can now be derived by applying the theory of Section 2.2 and assuming $\hat{h}_m(t)$ to be constant in time. This assumption will induce errors, as they are not constant in time. These errors are studied in Section 4.1.3, and by constraining the drive amplitudes to vary slowly enough, one can limit the errors to some finite magnitude.

As mentioned in Section 2.2.3, the effective Hamiltonian and its corresponding micromotion operator are given by $\hat{H}_{\text{eff}} = \sum_{k'\in\mathbb{N}} \hat{H}_{\text{eff}}^{(k')}$ and $\hat{S} = \sum_{k'\in\mathbb{N}} \hat{S}^{(k')}$, where $\hat{S}^{(k')}, \hat{H}_{\text{eff}}^{(k')} \propto 1/\omega_0^{k'}$. For some general rate $g = 1\,\text{GHz}$, $(g/\omega_0)^2 > 10^{-3}$ and $(g/\omega_0)^3 \ll 10^{-3}$, it seems appropriate to truncate these sums to $k' = 2$ as long as the rate of evolution under the Hamiltonian is less than g, i.e. $\hat{H}_{\text{eff}} = \sum_{k'=0}^{2} \hat{H}_{\text{eff}}^{(k')}$ and $\hat{S} = \sum_{k'=0}^{2} \hat{S}^{(k')}$, such that

$$\hat{H}_{\text{eff}} = \hat{h}_0 + \sum_{m\neq 0}\left(\frac{\left[\hat{h}_m, \hat{h}_{-m}\right]}{2m\omega_0} + \frac{\left[\left[\hat{h}_m, \hat{h}_0\right], \hat{h}_{-m}\right]}{2m^2\omega_0^2} + \sum_{l\neq m,0}\frac{\left[\left[\hat{h}_l, \hat{h}_{m-l}\right], \hat{h}_{-m}\right]}{3ml\omega_0^2}\right), \tag{4.9}$$

$$\hat{S}(t) = i\sum_{m\neq 0}\left(\frac{\hat{h}_m}{m\omega_0} + \frac{\left[\hat{h}_m, \hat{h}_0\right]}{m^2\omega_0^2} + \sum_{l\neq m,0}\frac{\left[\hat{h}_l, \hat{h}_{m-l}\right]}{2ml\omega_0^2}\right)e^{im\omega_0 t}, \tag{4.10}$$

also referred to as the second-order van Vleck expansion [35]. However, the expressions for the effective Hamiltonian at expansion order k' are increasingly complex, making it difficult to exactly predict the magnitudes of the neglected terms. Hence, this truncation will be further studied in Section 4.1.4.

4.1.3 Errors Induced by Slowly Varying Amplitudes

As the rotating terms $\hat{h}_k(t)$ are slowly varying with the time-dependent drive amplitudes, not constant, errors will be induced in the effective Hamiltonian at each perturbation order resulting from time-averaging. Most notably, the zeroth-order (RWA) effective Hamiltonian comes from

$$\hat{H}_{\text{eff}}^{(0)} = \frac{1}{T}\int_0^T \hat{H}_I(t)dt = \hat{h}_0(t), \tag{4.11}$$

which is not exactly true for time-dependent drive amplitudes. Noting that the period $T = 2\pi/\omega_0 \simeq 0.2393\,\mathrm{ns}$ is relatively short and the drive amplitudes are supposed to vary slowly, the drive amplitudes are expanded to linear-order as $v_m(t) \simeq v_m(t_0) + \dot{v}_m(t_0)(t - t_0), u_{n,m}(t) \simeq u_{n,m}(t_0) + \dot{u}_{n,m}(t_0)(t - t_0)$ for $t_0 < t < T + t_0$. Setting $t_0 = 0$, and assuming $|\dot{v}_m(0)|T, |\dot{u}_{n,m}(0)|T \ll 1$, gives $\hat{h}_k(t) \simeq (1 + \epsilon_k t)\hat{h}_k(0)$ for $0 < t < T$ where $\epsilon_k \hat{h}_k(0) = \partial_t \hat{h}_k|_{t=0}$. Since ϵ_k is proportional to all $\dot{v}_m(0), \dot{u}_{n,m}(0)$, it should satisfy $|\epsilon_k|T \ll 1$. Denoting $\hat{h}_k(0) = \hat{h}_k$ for simplicity, one can get the zeroth-order effective Hamiltonian from

$$\hat{H}_{\text{eff}}^{(0)} = \frac{1}{T}\int_0^T \hat{H}_I(t)dt = \frac{1}{T}\int_0^T \sum_{k=-12}^{12} (1 + \epsilon_k t)\hat{h}_k e^{ik\omega_0 t} dt, \tag{4.12}$$

which, under the simplification $\epsilon_k = \epsilon$, $\forall k$ gives

$$\hat{H}_{\text{eff}}^{(0)} = \hat{h}_0 + \frac{\epsilon}{\omega_0}\left(\pi\hat{h}_0 - i\sum_{k\neq 0}\frac{\hat{h}_k}{k}\right), \tag{4.13}$$

where $|\epsilon|/\omega_0 = |\epsilon|T/2\pi \ll 1$. If one assumes that $\epsilon \sim \dot{u}(0)$ for some arbitrary pulse amplitude $u(t)$, and imposes $|\dot{u}(0)|/\omega_0 < 10^{-3}$, then $\dot{u}(0)$ must be in the order of hundreds of MHz or less. Under this condition, (4.11) is a good approximation. Note that similar errors occur also for higher orders of the effective Hamiltonian, but since $\hat{H}_{\text{eff}}^{(k)} \propto 1/\omega_0^k$, these must be notably smaller than the errors for the zeroth-order. Hence, this chapter concludes that the effective Hamiltonian and its corresponding micromotion operator given in (4.9) and (4.10) should be valid if $\dot{v}_m, \dot{u}_{n,m} \lesssim 100\,\mathrm{MHz}$.

4.1.4 Effective Hamiltonian Accuracy

The effective Hamiltonian derived above includes analytical arguments for why truncating the sums in the full Hamiltonian and only including second-order perturbation terms gives a certain finite accuracy. These accuracies are here studied independently for the two truncated sums and the perturbative expansion by means of simulation of the system dynamics. Then, the two major limitations of the effective Hamiltonian are studied, namely, the pulse amplitudes and their rate of change.

4.1.4.1 Truncation of the Hilbert Space

To determine the truncation level of the Hilbert space for simulations, the method described in Section 3.1.3 is used. The pulses chosen for this simulation are

$$\xi(t) = -g_{1,1}^{\text{ac}} A(t)\cos(\omega_0 t), \quad \phi_e^{\text{ac}}(t) = \sum_{n=1}^{3} A(t)\cos(n\omega_0 t) \tag{4.14}$$

with $g_{1,1}^{\text{ac}}$ given in (2.53), for Gaussian pulse envelope

$$A(t) = \begin{cases} 2\pi \times 0.015 e^{-\frac{(t-t_0)^2}{2\sigma^2}}, & 0 \leq t \leq 60\,(\text{ns}) \\ 0, & \text{otherwise,} \end{cases} \tag{4.15}$$

with $t_0 = 30\,\mathrm{ns}$ and $\sigma = 10\,\mathrm{ns}$. This pulse is chosen because both charge and flux pulses of all three frequencies are applied, and the amplitude and duration are representative for typical pulses that are considered in this thesis. Note that the amplitude of $\xi(t)$ is chosen so that it approximately cancels the displacement of the $1\omega_0$-flux pulse, since the state will be heavily displaced even for small values $1\omega_0$-flux pulse and thus require a very large Hilbert space. The Hamiltonian used for simulation is given by

$$\hat{H}(t) = \omega_0 \hat{a}^\dagger \hat{a} + \xi(t)(\hat{a}^\dagger + \hat{a}) + \sum_{k=1}^{6} g_k(t)(\hat{a}^\dagger + \hat{a})^k, \quad g_k(t) = \frac{\varphi_{zpf}^k}{k!}\left(\frac{\partial^k U}{\partial \varphi^k}\right)_{\varphi_m, \phi_e}, \tag{4.16}$$

with $\phi_e = \phi_e^{\mathrm{dc}} + \phi_e^{\mathrm{ac}}(t)$, $\phi_e^{\mathrm{dc}} = 0.3912 \times 2\pi$. Note that this is equivalent to keeping all orders in the ac-flux expansion, i.e. $M \to \infty$. The simulation is then performed by letting an initial state $|\psi(t=0)\rangle = |0\rangle$ evolve under the Schrödinger equation $i\partial_t |\psi(t)\rangle = \hat{H}(t) |\psi(t)\rangle$.

The simulated results are presented in Fig. 4.1 showing $1 - \mathcal{F}(n)$ and $1 - \mathcal{F}_{N=400}(n)$ for $n = 3, ..., 100$. As one can see, both measures $\mathcal{F}(n)$ and $\mathcal{F}_{N=400}(n)$ increase steadily until $n = 42$. After that point, both measures fluctuate between values of roughly $1 - 10^{-4}$ to $1 - 10^{-8}$. The reason why they do fluctuate is likely related to errors in the simulation or the normalization of truncated vectors. It may be wise to choose $N_{dim} > 42$, to safeguard for pulses that generate states with higher occupation for larger Fock states. Hence, it seems reasonable to choose $N_{dim} = 60$. This truncation is used for all remaining simulations in this section.

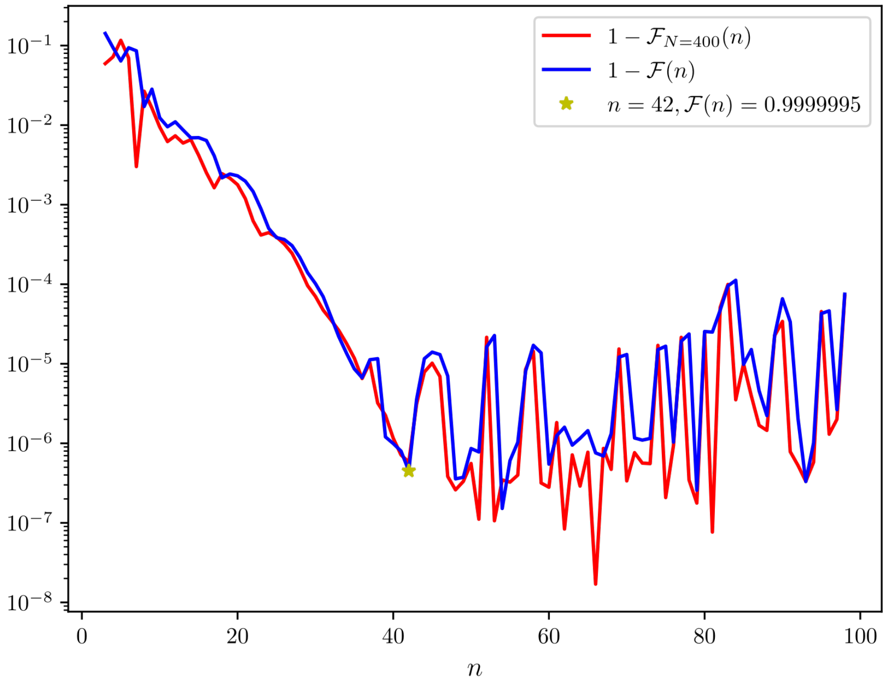

Figure 4.1: $1 - \mathcal{F}(n)$ and $1 - \mathcal{F}_{N=400}(n)$ for $n = 3, ..., 100$ in logarithmic scale. Both measures increase until $n = 42$, which is noted as a star in the plot.

4.1.4.2 Truncation of the Full Hamiltonian

In Section 4.1.1, the two sums of the Hamiltonian in (2.52) are truncated to $N = 6$, $M = 2$ giving (4.4). To measure the accuracy of the first truncation, $N = 6$, the Hamiltonians

$$\hat{H}_N(t) = \omega_0 \hat{a}^\dagger \hat{a} + \xi(t)(\hat{a}^\dagger + \hat{a}) + \sum_{k=1}^{N} g_k(t)(\hat{a}^\dagger + \hat{a})^k, \quad g_k(t) = \frac{\varphi_{zpf}^k}{k!}\left(\frac{\partial^k U}{\partial \varphi^k}\right)_{\varphi_m, \phi_e} \tag{4.17}$$

for $N = 4, ..., 7$ are used to perform the same simulations as in the section above, with initial states $|\psi_N(t=0)\rangle = |0\rangle$ and pulses given by (4.14). This results in four states $|\psi_N(t=60)\rangle$, $N = 4, ..., 7$, and the accuracy of the truncation can be measured by the overlaps of the states for $N = 4, 5, 6$ to $N = 7$. This gives the following overlaps: $|\langle\psi_4|\psi_7\rangle|^2 \simeq 0.985743$, $|\langle\psi_5|\psi_7\rangle|^2 \simeq 0.985074$ and $|\langle\psi_6|\psi_7\rangle|^2 \simeq 0.999442$. Moreover, $|\langle\psi_4|\psi_5\rangle|^2 \simeq 0.971107$ and $|\langle\psi_5|\psi_6\rangle|^2 \simeq 0.985827$. This shows that the terms of $N \geq 7$ are negligible and that $N = 6$ is indeed an appropriate truncation. The Wigner plots for $N = 4, ..., 7$ are shown in Fig. 4.2.

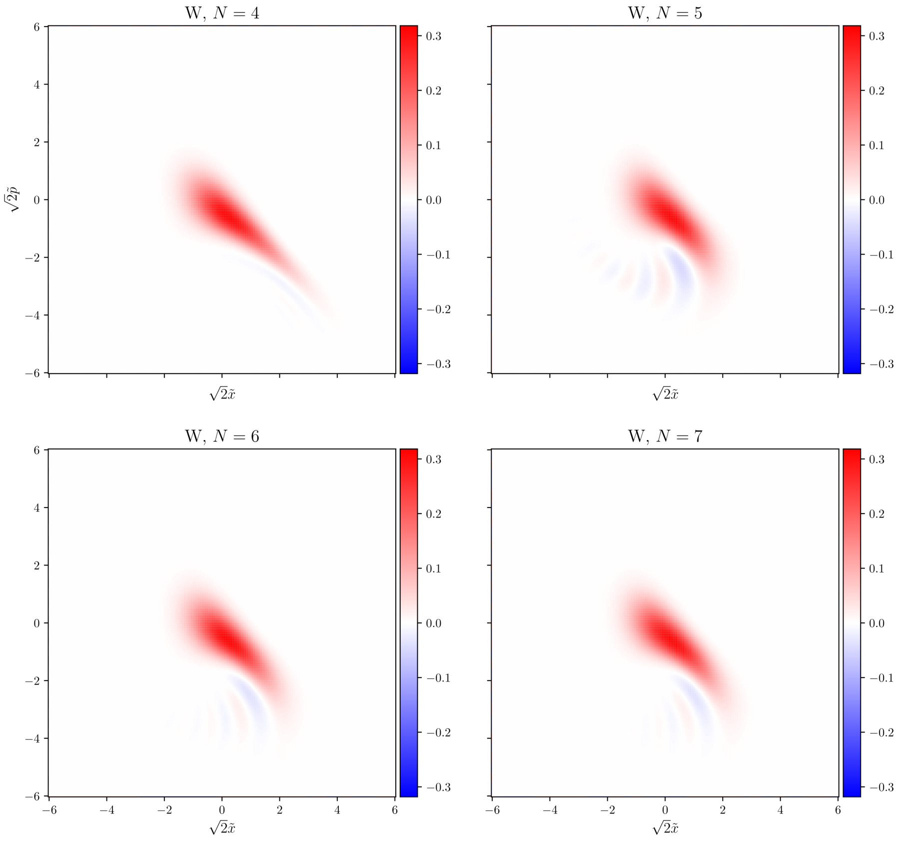

Figure 4.2: Wigner functions for $N = 4, ..., 7$, i.e. the states $|\psi_4\rangle, ..., |\psi_7\rangle$.

For the second truncation, $M = 2$, one can compare the Hamiltonian

$$\hat{H}_M(t) = \omega_0 \hat{a}^\dagger \hat{a} + \xi(t)(\hat{a}^\dagger + \hat{a}) + \sum_{k=1}^{6}\sum_{j=1}^{M}(g_k^{\mathrm{dc}} + g_{k,j}^{\mathrm{ac}} \phi_e^{\mathrm{ac}}(t)^j)(\hat{a}^\dagger + \hat{a})^k \tag{4.18}$$

to $\hat{H}_{N=6}(t)$, which in the limit $M \to \infty$ are exactly equal. Performing exactly the same simulations as above for $M = 1, 2, 3$ gives three new states $|\psi_{6,1}\rangle$, $|\psi_{6,2}\rangle$, $|\psi_{6,3}\rangle$. To measure the accuracy of this truncation, one can calculate their overlap to $|\psi_6\rangle$, which gives $|\langle\psi_{6,1}|\psi_6\rangle|^2 \simeq 0.941827$, $|\langle\psi_{6,2}|\psi_6\rangle|^2 \simeq 0.997165$ and $|\langle\psi_{6,3}|\psi_6\rangle|^2 \simeq 1.00000$. From this it is clear that $M = 2$ is a good approximation, but also that $M = 3$ is much better. However, it is difficult to include $\phi_e^{\mathrm{ac}}(t)^3$ in the effective Hamiltonian, so it is for now decided that $M = 2$ is adequate. The Wigner plots for $M = 1, 2, 3$ are shown in Fig. 4.3.

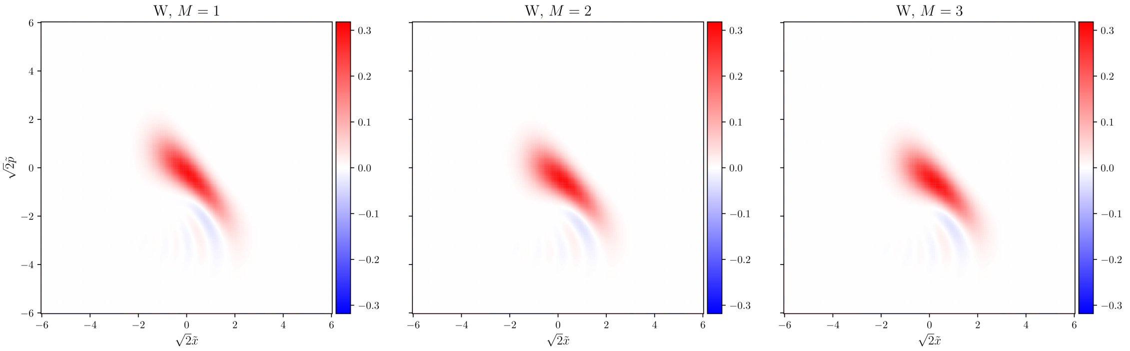

Figure 4.3: Wigner functions for $M = 1, 2, 3$, i.e. the states $|\psi'_1\rangle$, $|\psi'_2\rangle$, $|\psi'_3\rangle$.

4.1.4.3 Perturbative Expansion Order

In Section 4.1.2, the effective Hamiltonian and its corresponding micromotion operator were presented in (4.9) and (4.10) to include terms up to order $1/\omega_0^2$. Here, the accuracy of the effective Hamiltonian is studied by simulating the system for $\hat{H}_{\mathrm{eff},0}$, $\hat{H}_{\mathrm{eff},1}$ and $\hat{H}_{\mathrm{eff},2}$, where $\hat{H}_{\mathrm{eff},k}$ is the effective Hamiltonian including terms up to order $1/\omega_0^k$, derived using $N = 6, M = 2$ in the expansion of the full Hamiltonian. More precisely, the exact same simulation as above is performed, but according to (2.27), by letting the initial state $\exp\left\{-i\hat{S}_k(t = 0)\right\}|0\rangle$ evolve under $\hat{H}_{\mathrm{eff},k}(t)$ from $t = 0$ to $t = 60$, resulting in a set of states $|\psi'_k\rangle$. The final states are then given by $|\psi_{\mathrm{eff},k}\rangle = \exp\left\{i\hat{S}_k(t = 60)\right\}|\psi'_k\rangle$, and their Wigner plots are shown in Fig. 4.4. The effective Hamiltonian is formally derived from $\hat{H}_{M=2}(t)$, but is ultimately also an approximation of $\hat{H}_{N=6}(t)$. Thus, one would like to compare the effective Hamiltonian to both of these. This is done by calculating the overlap for $|\psi_{\mathrm{eff},k}\rangle$ to $|\psi_{6,2}\rangle$ and $|\psi_6\rangle$. For $\hat{H}_{M=2}(t)$, this gives $|\langle\psi_{\mathrm{eff},0}|\psi_{6,2}\rangle|^2 \simeq 0.688971$, $|\langle\psi_{\mathrm{eff},1}|\psi_{6,2}\rangle|^2 \simeq 0.994239$ and $|\langle\psi_{\mathrm{eff},2}|\psi_{6,2}\rangle|^2 \simeq 0.999502$. For $\hat{H}_{N=6}(t)$, the overlaps are $|\langle\psi_{\mathrm{eff},0}|\psi_6\rangle|^2 \simeq 0.683113$, $|\langle\psi_{\mathrm{eff},1}|\psi_6\rangle|^2 \simeq 0.992798$ and $|\langle\psi_{\mathrm{eff},2}|\psi_6\rangle|^2 \simeq 0.995452$. This shows, that for the given pulse, only including terms up to order $1/\omega_0$ is already a good approximation. It also indicates that, in order to achieve a more accurate effective Hamiltonian, the next step would be to use the truncation $M = 3$ rather than including terms up to order $1/\omega_0^3$ in the effective Hamiltonian, since $1 - |\langle\psi_{\mathrm{eff},2}|\psi_{6,2}\rangle|^2 < 10^{-3}$ but $1 - |\langle\psi_{6,2}|\psi_6\rangle|^2 > 10^{-3}$. In other words, $\hat{H}_{\mathrm{eff},2}$ is a much better approximation of $\hat{H}_{M=2}$, than $\hat{H}_{M=2}$ is of $\hat{H}_{N=6}$. The comparison between $\hat{H}_{\mathrm{eff},1}$, $\hat{H}_{\mathrm{eff},2}$, $\hat{H}_{M=2}$ and $\hat{H}_{N=6}$ will be further studied in the next subsection.

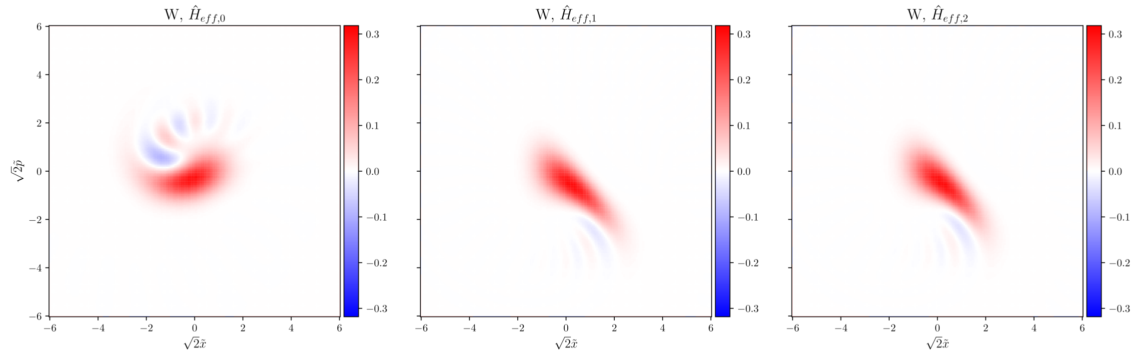

Figure 4.4: Wigner functions for $\hat{H}_{\text{eff},k}$, $k = 0, 1, 2$, i.e. the states $|\psi_{\text{eff},0}\rangle$, $|\psi_{\text{eff},1}\rangle$, $|\psi_{\text{eff},2}\rangle$.

4.1.4.4 Bound on Pulse Amplitude

As mentioned in Section 4.1.1, the accuracy of the Hamiltonian is dependent on ϕ_e^{ac} being small. More precisely $|\phi_e^{\text{ac}}(t)| \leq 0.03697 \times 2\pi$ at all times t ensures that $g_{k,M+1}^{\text{ac}}|\phi_e^{\text{ac}}(t)^M|/g_{k,1}^{\text{ac}} < 10^{-3}\ \forall k$. Moreover, the effective Hamiltonian is derived under the assumption that the driving strength is small enough that $\left\|\hat{h}_k\right\|/\omega_0 \ll 1,\ \forall k$, ensuring that its accuracy increases with each expansion order. The norm $\left\|\hat{h}_k\right\|$ is not properly defined here, but note that it must consider that the average occupation number for the state of the system is low. The accuracy of $\hat{H}_{M=2}$ and $\hat{H}_{\text{eff}}$ are thus limited by the amplitude of the applied pulses.

To measure this dependence, one can redefine the pulse envelope from (4.15) to

$$A(t, r) = \begin{cases} 2\pi \times r e^{-\frac{(t-t_0)^2}{2\sigma^2}}, & 0 \leq t \leq 60\,(\text{ns}) \\ 0, & \text{otherwise}, \end{cases} \tag{4.19}$$

where $t_0 = 30\,\text{ns}$ and $\sigma = 10\,\text{ns}$. Then, one can perform the same simulations as before for $r \in [0.005, 0.030]$, resulting in the set of states $|\psi_6(r)\rangle$ for $\hat{H}_{N=6}$, $|\psi_{6,2}(r)\rangle$ for $\hat{H}_{M=2}$, $|\psi_{\text{eff},1}(r)\rangle$ for $\hat{H}_{\text{eff},1}$ and $|\psi_{\text{eff},2}(r)\rangle$ for $\hat{H}_{\text{eff},2}$. The overlaps between $|\psi_6(r)\rangle$ and the remaining states are shown in Fig. 4.5. From this, one can see that $\hat{H}_{\text{eff},2}$ emulates $\hat{H}_{N=6}$ very well for amplitude $r \lesssim 0.010 \times 2\pi$, but starts to perform poorly for $r \gtrsim 0.015 \times 2\pi$. Hence, the amplitude should be kept below this to ensure that the effective Hamiltonian is accurate.

Moreover, one can notice that both $|\langle\psi_{\text{eff},1}|\psi_6\rangle|^2$ and $|\langle\psi_{\text{eff},2}|\psi_6\rangle|^2$ are very close to $|\langle\psi_{6,2}|\psi_6\rangle|^2$. This further strengthens the argument in Section 4.1.4.3, that to increase the accuracy of the effective Hamiltonian one should truncate the ac-flux expansion at $M = 3$ rather than including the third-order perturbative expansion terms.

Lastly, the results show that $\hat{H}_{\text{eff},1}$ and $\hat{H}_{\text{eff},2}$ perform almost equally well for $r \lesssim 0.015 \times 2\pi$. So in this regime, $\hat{H}_{\text{eff},1}$ can be used to reduce the computational cost of simulation without losing much accuracy.

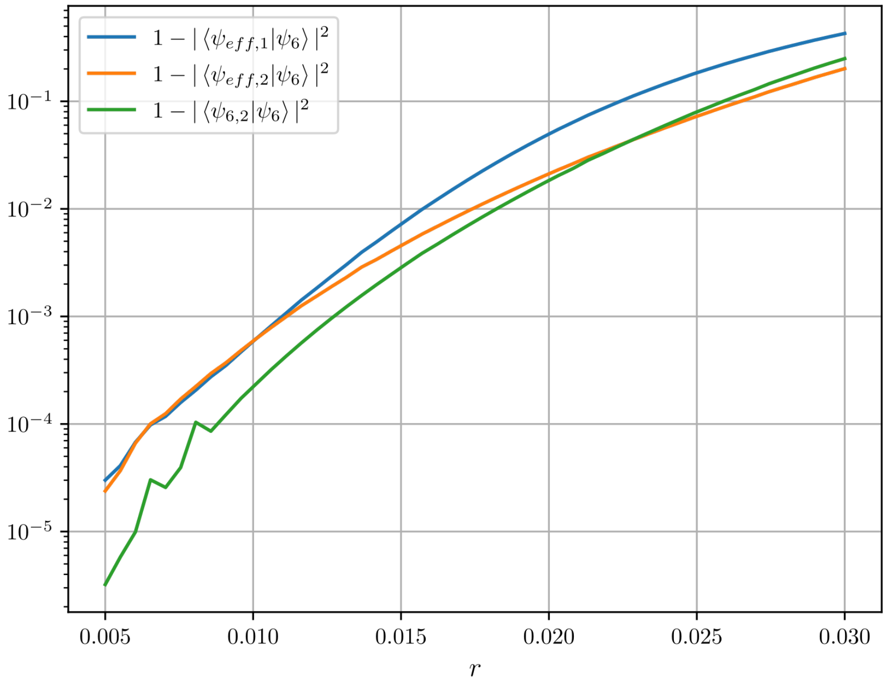

Figure 4.5: Overlaps between the four states on a logarithmic scale for amplitudes $r \in [0.005, 0.030]$.

4.1.4.5 Rise and Fall Time Limitation

In Section 4.1.3, it is shown that the rate of change of the pulse amplitudes induces errors in the effective Hamiltonian. An approximate bound on the rate of change is derived to limit these errors. However, this derivation involves the assumptions that the rate of change of each $\hat{h}_k$ is similar to the rate of change of the pulse amplitudes and that it is the same for each k. As this is not necessarily true or easy to check analytically, this is tested by simulating pulses with different rise and fall times. A longer rise (or fall) time is of course equivalent to a slower rate of change, and vice versa.

To do this, the pulse envelope will again be redefined. This time as

$$A(t, t_{flat}) = \begin{cases} 2\pi \times 0.015 e^{-\frac{(t-t_0+t_{flat}/2)^2}{2\sigma^2 b(t_{flat})}}, & 0 \leq t < 30 - t_{flat}/2 \\ 2\pi \times 0.015, & 30 - t_{flat}/2 \leq t < 30 + t_{flat}/2 \\ 2\pi \times 0.015 e^{-\frac{(t-t_0-t_{flat}/2)^2}{2\sigma^2 b(t_{flat})}}, & 30 + t_{flat}/2 \leq t \leq 60 \\ 0, & \text{otherwise}, \end{cases} \tag{4.20}$$

where $t_0 = 30\,\text{ns}$, $\sigma = 10\,\text{ns}$, $t_{flat} \in [0, 22]\,\text{ns}$ is some time for which the envelope is flat, and $b(t_{flat})$ is a parameter determined such that

$$\int_0^{60} A(t, t_{flat})dt = \int_0^{60} A(t, 0)dt, \tag{4.21}$$

i.e. the effective gate duration is always the same. When increasing t_{flat}, the rise time of the pulse envelope decreases since the width of the Gaussian function,

$\sigma\sqrt{b(t_{flat})}$, decreases. To measure how t_{flat} affects the accuracy of the effective Hamiltonian, one can perform the exact same simulations as in the previous subsection, resulting in a set of states $|\psi_6(t_{flat})\rangle$, $|\psi_{6,2}(t_{flat})\rangle$, $|\psi_{\text{eff},1}(t_{flat})\rangle$ and $|\psi_{\text{eff},2}(t_{flat})\rangle$. The overlaps between these states are shown in Fig. 4.6.

From these results, one can note that the effective Hamiltonians are accurate even for faster rise and fall times. This is likely an effect of the pulse amplitudes already being limited to be small, since even if the rise time is equal to the period of the oscillator, $T = 2\pi/\omega_0$, the rate of change will be small: $\dot{A}(t)T \simeq 0.015 \times 2\pi \ll 1$.

The results also show that the accuracy of the effective Hamiltonians decrease with the accuracy of $\hat{H}_{M=2}$. This is likely an effect of the amplitude being large for a longer duration as the flat duration increases, and at larger amplitudes $\hat{H}_{M=2}$ is an increasingly worse approximation. Hence, most of the decrease in accuracy of the effective Hamiltonians can be attributed to that of $\hat{H}_{M=2}$, rather than the actual rise and fall times themselves.

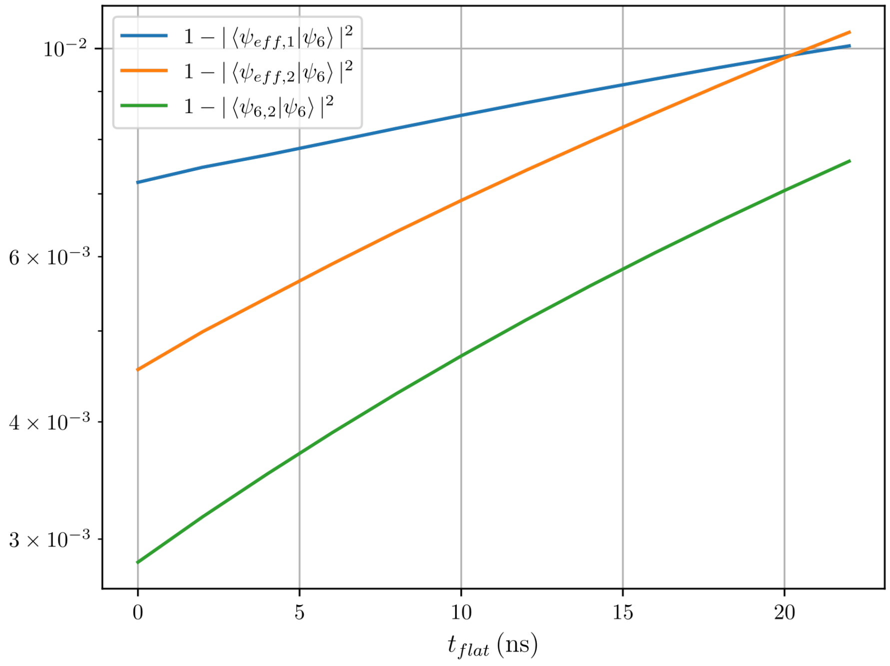

Figure 4.6: Overlaps between the four states on a logarithmic scale for $t_{flat} = 0, 2, 4, ..., 22$.

4.2 Optimal Control

In this section, cubic phase states and cat states are generated by means of optimal control. In both cases, this is done by using the effective Hamiltonian $\hat{H}_{\text{eff},1}$ and a Hilbert space truncated at $N_{dim} = 42$ in order to speed up the optimization. The cut-off frequency of the filtering function is set to $\omega_c = 200\,\text{MHz}$ and the Gaussian envelopes are defined to have center time $t_0 = T_{dur}/2$ and flat duration $t_{flat} = 2T_{dur}/3$, with the exception of Section 4.2.1.1. The flux bias point is set to $\phi_e^{\mathrm{dc}} = 0.391028 \times 2\pi$ to cancel Kerr effects. The found pulses are analyzed by comparing the fidelity to the target states for both $\hat{H}_{\mathrm{eff},1}$ and the full Hamiltonian $\hat{H}_{N=6}$.

During the initial attempts of optimizing the pulses, it appeared that the optimizer consistently chose to heavily displace the state, which consequently pushed it out of the computational basis. As no efficient solution was found to remedy this, the $1\omega_0$ flux and charge pulses were defined to always cancel each others displacement. This clearly limits the control of the system. It is not, however, a problem for the cubic phase state. For the cat state, it is taken into account by using different initial states.

4.2.1 Cubic Phase States

The optimal control methods in Section 3.2 are first used to generate a cubic phase state. First, by tuning the amplitude and phases of a specific set of pulses, and then by pulse shaping. Generating the state from pulse shaping shows that it is possible to generate non-Gaussian states by full optimal control. Lastly, the pulses found are tested in terms of robustness to deviations in Hamiltonian parameters.

In both cases, the maximum amplitudes of the flux pulses were set to be $0.015 \times 2\pi$ as a result of Section 4.1.4.4 and the total duration to 60 ns.

4.2.1.1 Optimizing the Cubic Phase Gate

In Eriksson et al. [13], a cubic phase state was experimentally realized by first applying a squeezing ($2\omega_0$) flux pulse for 20 ns, followed by $1\omega_0$ and $3\omega_0$ flux pulses and a $1\omega_0$ charge pulse for 40 ns. The amplitudes and phases of the pulses were calibrated such that the displacement of the $1\omega_0$ pulses cancel and to achieve desired squeezing ζ and cubicity κ. The closest pure cubic phase state to the measured state was then found with 92% fidelity, with $\zeta = -0.61$ and $\kappa = 0.11$.

A relatively simple optimal control problem can be defined by recreating the above result in simulation by means of optimal control, rather than manual calibration. However, due to differing definitions, the target state is chosen as $\zeta = -0.61, \kappa = -0.11$. To this end, following the notation of Section 3.2, the number of segments was chosen as $N_s = 2$, with respective durations $T_1 = 20\,\mathrm{ns}$ and $T_2 = 40\,\mathrm{ns}$. The set of pulses chosen were a $2\omega_0$ flux pulse $u_2(t)$, $1\omega_0$ and $3\omega_0$ flux pulses $u_1(t)$ and $u_3(t)$, and $1\omega_0$ charge pulse $v(t)$. The amplitudes were then fixed such that $u_1(t), u_3(t), v(t) = 0$ for $t < T_1$, and $u_2(t) = 0$ for $t > T_1$. Furthermore, in order to enforce the cancellation of displacement of the two $1\omega_0$ pulses, the amplitude and phase of the charge pulse was fixed such that $v(t) = -g_{1,1}^{\mathrm{ac}} u_1(t)$. Hence, the six remaining optimization variables were the amplitudes and phases of $u_1(t), u_2(t)$ and $u_3(t)$. The number of test points chosen at each iteration is $\lambda = 40$. Since the amplitudes were fixed to be non-zero in only one segment each, the pulse amplitudes were not filtered and the Gaussian envelope was defined so that the amplitudes were tied to zero in $t = 0, T_1, T_1 + T_2$. This means that for $u_2(t)$, a Gaussian envelope with $t_0 = T_1/2$ and $t_{flat} = 2T_1/3$ was applied. For the remaining pulses, $t_0 = T_1 + T_2/2$, $t_{flat} = 2T_2/3$.

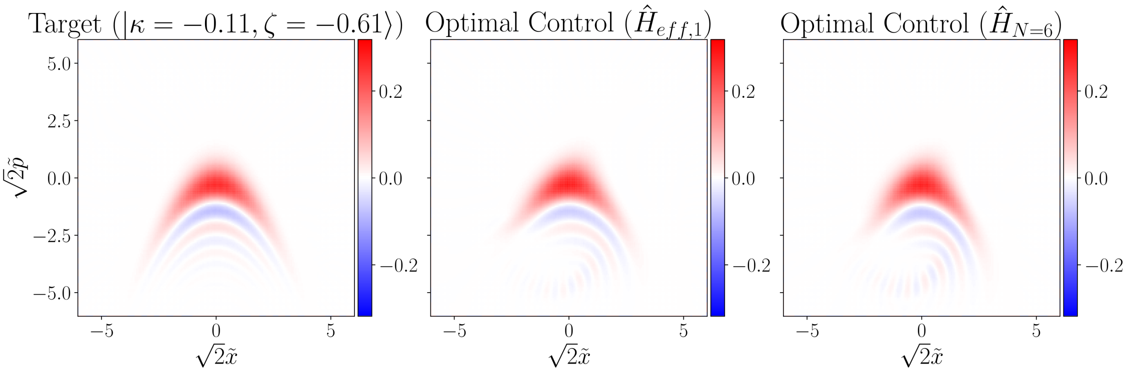

Figure 4.7: Wigner functions of the target cubic phase state $|\kappa = -0.11, \zeta = -0.61\rangle$ (left), and the states generated by the optimized pulses for $\hat{H}_{\mathrm{eff},1}$ (center) and $\hat{H}_{N=6}$ (right), in a Hilbert space truncated at $N_{dim} = 100$.

For a maximum number of iterations $N_{max} = 500$ and target cost $C_{target} = 0.01$, the minimum cost was found to be $C_{opt} = 0.01247$ (which was found already after $N_{iter} = 211$ iterations). By simulating the full Hamiltonian ($\hat{H}_{N=6}$) with the same pulses, the overlap to the effective Hamiltonian is 0.98058 resulting in the overlap 0.97263 to the target state. The Wigner functions of the target state, as well as the simulated states using the effective and full Hamiltonians are shown in Figure 4.7. Note that a lower C_{opt} could have probably been achieved by being more careful with fixing the amplitude and phase of the charge pulse. Simply setting $v(t) = -g^{\mathrm{ac}}_{1,1}u_1(t)$ means that only the zeroth order (in $1/\omega_0$) displacement contributions from $u_1(t)$ are taken into account. For example, by including first order corrections to the RWA, one can find a displacement contribution proportional to $g^{\mathrm{ac}}_{1,1}g^{\mathrm{dc}}_4/\omega_0 \sim 1\,\mathrm{MHz}$. However, even with $C_{opt} = 0$ the overlap for the full Hamiltonian to target would still not surpass 0.98058, and hence $v(t) = -g^{\mathrm{ac}}_{1,1}u_1(t)$ was deemed sufficient.

4.2.1.2 Pulse Shaping Optimization

After the above results, it is also of interest to see if one could generate the same cubic phase state without strictly enforcing the optimizer to first squeeze the vacuum state and then perform a cubic phase gate. In other words, try to generate the target cubic phase state by pulse shaping $u_1(t)$, $u_2(t)$ and $u_3(t)$, with $v(t) = -g^{\mathrm{ac}}_{1,1}u_1(t)$. The total duration of the pulses was set to $T_{dur} = 60\,\mathrm{ns}$, which was split into $N_s = 6$ even segments of duration $T_i = 10\,\mathrm{ns}$, $i = 1, ..., 6$. Thus, the optimization were set to be the amplitude of each pulse in each segment, as well as their overall phase, amounting to 21 variables in total. The number of test points chosen at each iteration is $\lambda = 100$. The pulses were then filtered and multiplied by a Gaussian envelope as described in Section 3.2. With a target cost $C_{target} = 0.005$, the optimizer reached $C_{opt} = 0.004965$ in $N_{iter} = 583$ iterations. However, the overlap between the simulated states from $\hat{H}_{\mathrm{eff},1}$ and $\hat{H}_{N=6}$ was 0.949591 when applying the found pulses. As a result, the overlap between the target state and the simulated state from $\hat{H}_{N=6}$ was only 0.950428. The Wigner functions of the simulated states are shown in Figure 4.8. The shaped pulse amplitudes that were found in the optimization are

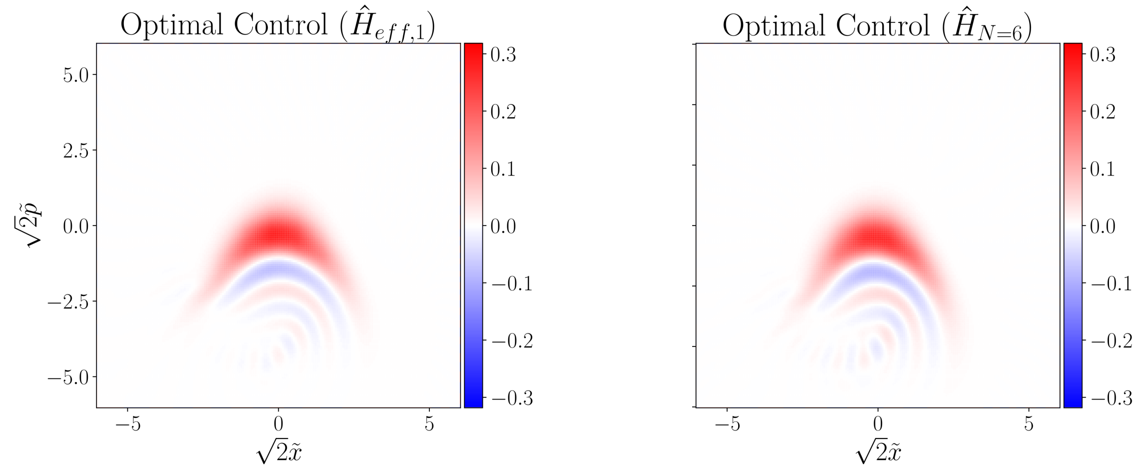

Figure 4.8: Wigner functions of the states generated by the shaped pulses for $\hat{H}_{\text{eff},1}$ (left) and $\hat{H}_{N=6}$ (right), in a Hilbert space truncated at $N_{dim} = 100$.

shown in Figure 4.9.

4.2.1.3 Parameter Robustness

In a realistic experimental setup, the Hamiltonian of the SNAIL-resonator will deviate from the ideal, full Hamiltonian. There will always be some uncertainty for the measured and designed circuit parameters, and the SNAIL-resonator will be coupled to a read-out qubit which will slightly shift the Hamiltonian parameters. Hence, one would like to study how robust the found pulses are to deviations of the Hamiltonian parameters. Here, the effect of deviations up to 5% in the parameters $g_3^{\text{dc}}, g_4^{\text{dc}}, g_{1,1}^{\text{ac}}, g_{2,1}^{\text{ac}}$ and $g_{3,1}^{\text{ac}}$ will be studied, as well as deviations in frequency (ω_0) and Kerr ($K^{(2)}$) in the range of hundreds of kHz will be studied. This will be done for both the tuned pulses found in Sections 4.2.1.1 and 4.2.1.2, from here on referred to the *standard pulses* and *shaped pulses* respectively.

To study this, the following method is used. For a parameter p, the parameter instead takes the value $p' = p + \Delta p$, where Δp is swept over a range of values. For each value of p', the new optimal bias point is found (except $\omega_0, g_{1,1}^{\text{ac}}, g_{2,1}^{\text{ac}}, g_{3,1}^{\text{ac}}$ as it does not change), and the Hamiltonian is redefined. The time evolution of the system is then simulated, both using the standard and shaped pulses, with the redefined Hamiltonian. The fidelity (state overlap) to the target cubic phase state is then calculated.

The results show that the pulses are more resilient to deviations in Kerr than to frequency, as seen in Figure 4.10. However, one can also notice that the shaped pulses are more susceptible to changes in frequency than the standard pulses. For g_3^{dc} and g_4^{dc}, Figure 4.11 shows that both sets of pulses are very robust towards changes in g_4^{dc}, and slightly less so towards changes in g_3^{dc}. Moreover, one can note that the fidelity increases with higher values of g_3^{dc}. The fidelities for deviated values of $g_{1,1}^{\text{ac}}$, $g_{2,1}^{\text{ac}}$, $g_{3,1}^{\text{ac}}$ are shown in Figure 4.12. From these heatmaps, one can notice that the pulses are generally robust towards deviations up to 5% in these parameters. Additionally, the standard pulses seem to give higher fidelity for deviated parameters, especially an

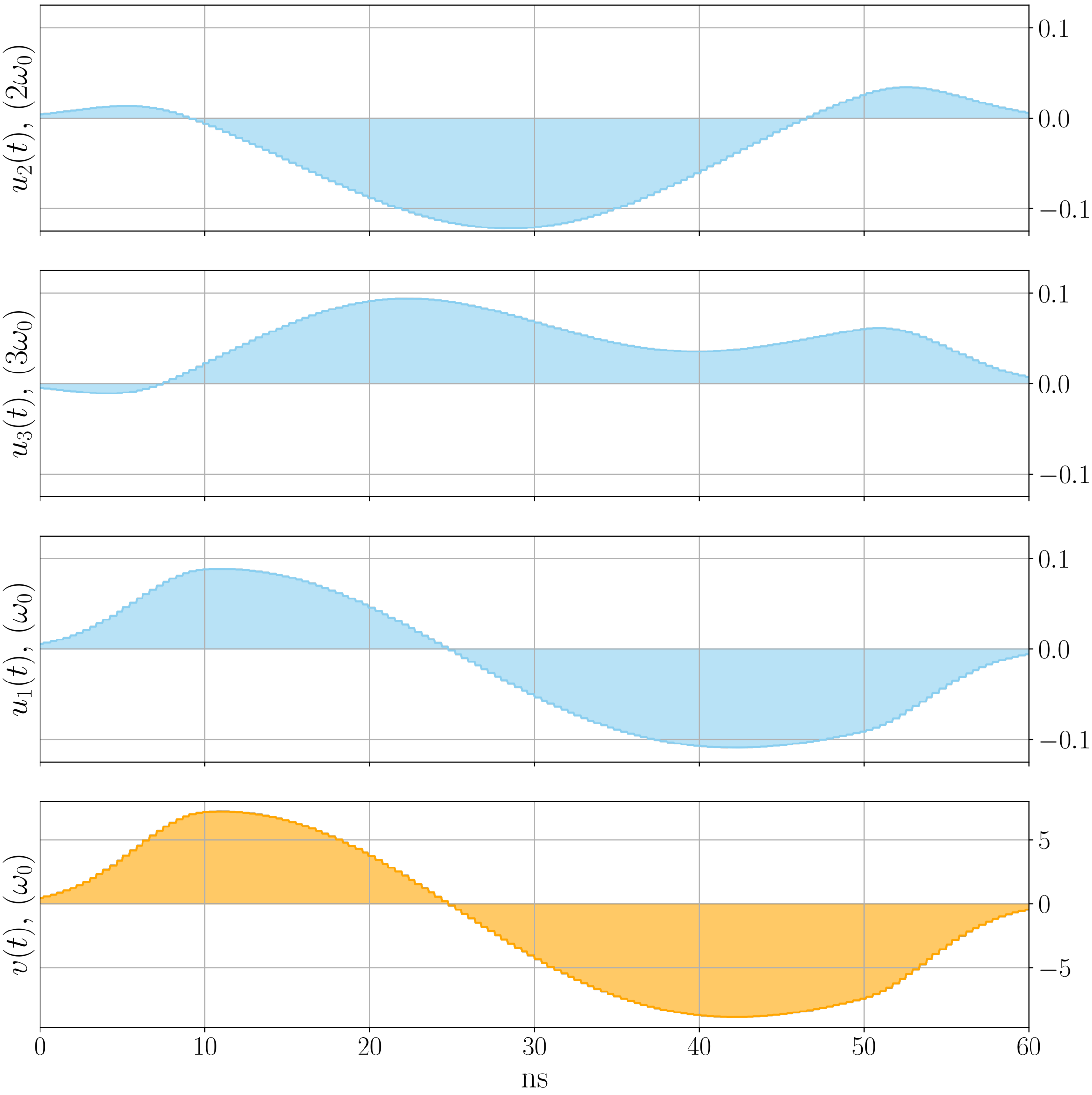

Figure 4.9: Pulse amplitudes found to generate the target cubic phases state in pulse shaping optimization. Flux pulses are blue in color, and the charge pulse is orange.

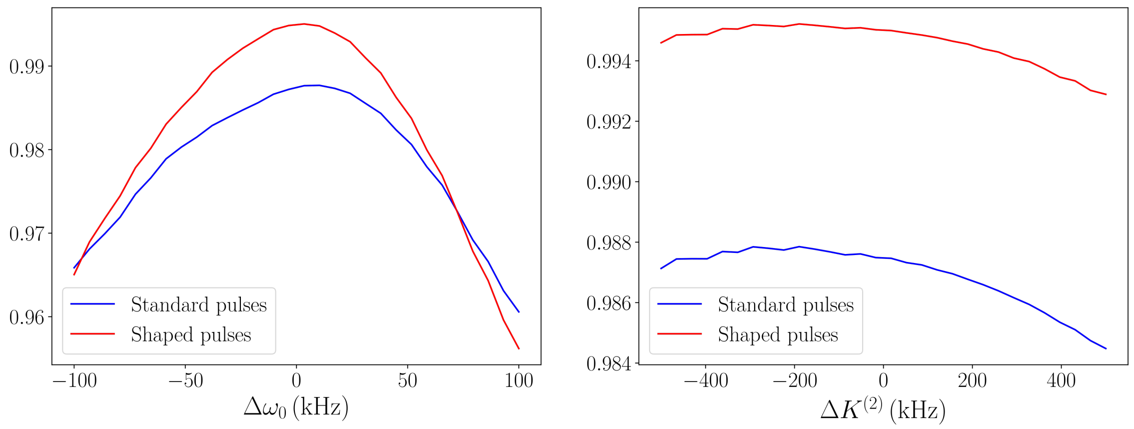

Figure 4.10: Fidelity of standard and shaped pulses for deviated values of frequency ω_0 (left) and Kerr $K^{(2)}$ (right).

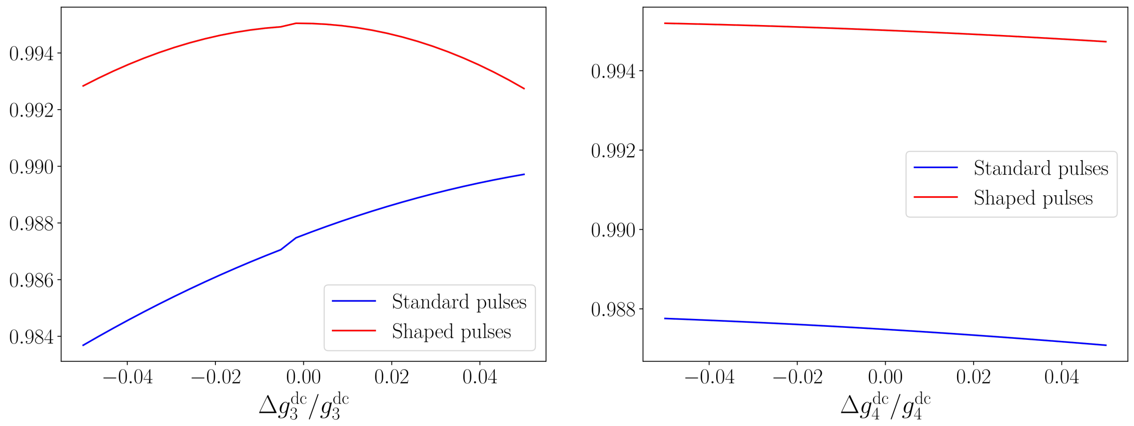

Figure 4.11: Fidelity of standard and shaped pulses for deviated values of g_3^{dc} (left) and g_4^{dc} (right).

increased $g_{1,1}^{\mathrm{ac}}$.

4.2.2 Cat States

Here, cat states are generated by means of optimal control. In contrast to previous optimizations, the optimizable pulses are chosen to be $u_n^{(r)}(t) = A_n^{(r)}(t)\cos(n\omega_0 t)$ and $u_n^{(i)}(t) = A_n^{(i)}(t)\cos(n\omega_0 t + \pi/2)$ for $n = 1, 2, 3$, where $A_n^{(r/i)}(t)$ are the pulse amplitudes. Again, the charge pulses are defined such that $v^{(r/i)}(t) = -g_{1,1}^{\mathrm{ac}} u_1^{(r/i)}(t)$. Since there are now 2 pulses for each frequency, the maximum amplitude is set to $0.015 \times 2\pi/\sqrt{2}$. The total duration of the pulses is set to 120 ns, evenly split into $N_s = 12$ segments of duration $T_i = 10$ ns for all i. The number of optimization variables hence grows to 72, and the number of test points for each iteration is chosen to $\lambda = 200$.

The optimization variables are chosen as above due to the fact that all leading-order driven terms in the effective Hamiltonian will be proportional to $A(t)e^{\pm i\theta}$ if the pulses are of the type $A(t)\cos(n\omega_0 + \theta)$. These terms are hence confined to a line in the

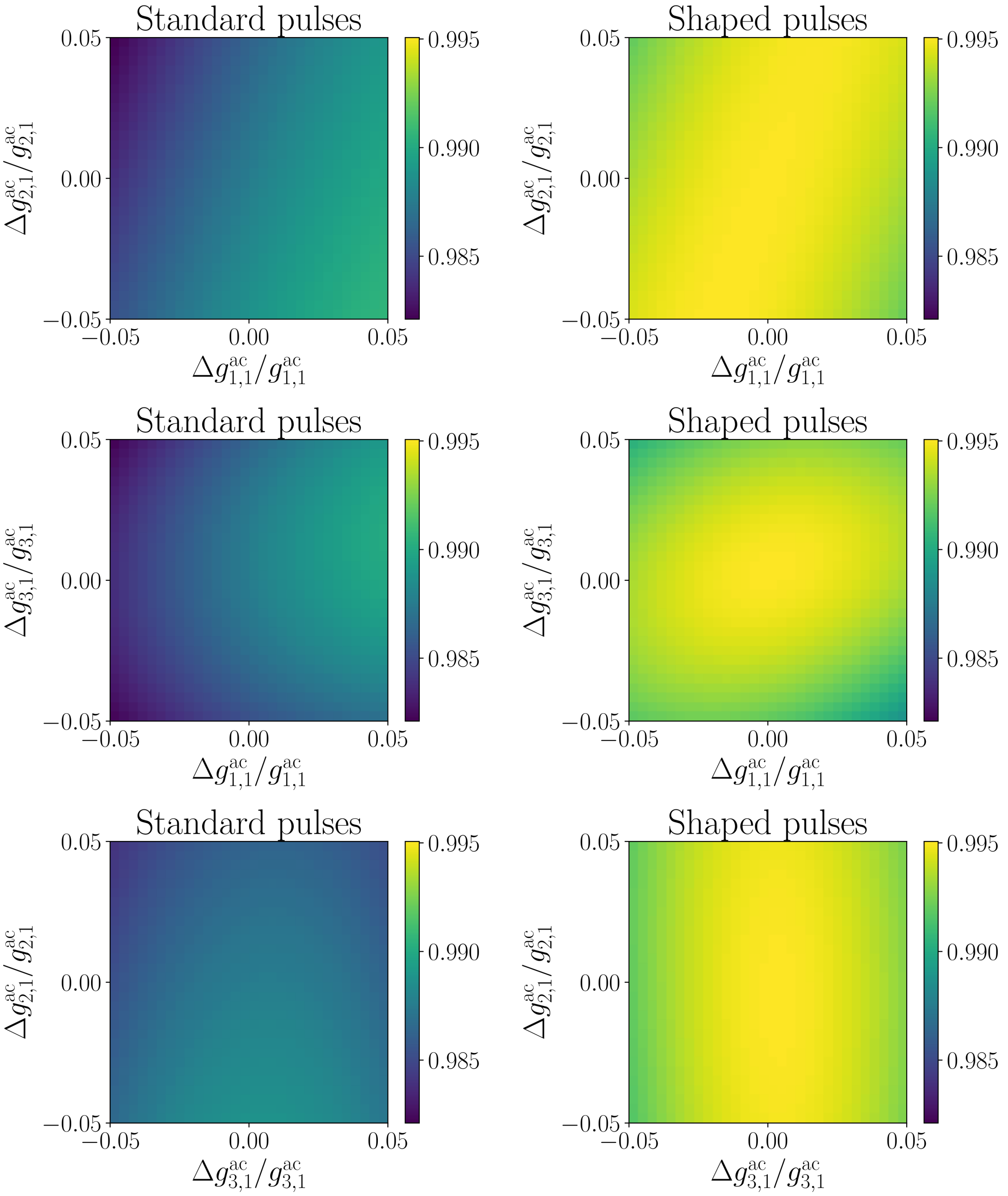

Figure 4.12: Heatmaps showing fidelity of standard and shaped pulses for deviated values of $g^{\text{ac}}_{1,1}$, $g^{\text{ac}}_{2,1}$, $g^{\text{ac}}_{3,1}$.

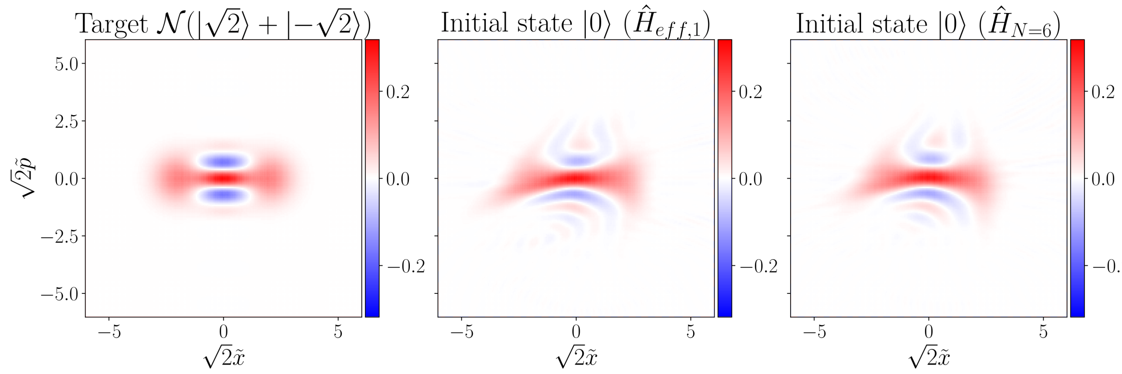

Figure 4.13: Wigner functions of the target cat state $\mathcal{N}(\left|\sqrt{2}\right\rangle + \left|-\sqrt{2}\right\rangle)$ (left), and the states generated by the optimized pulses for $\hat{H}_{\text{eff},1}$ (center) and $\hat{H}_{N=6}$ (right) with the initial state $|0\rangle$, in a Hilbert space truncated at $N_{dim} = 100$.

complex plane. By applying two pulse of the same frequency, but choosing $\theta = 0$ for one and $\theta = \pi/2$ for the other, the terms are instead proportional to $A^{(r)}(t) \pm iA^{(i)}(t)$, which spans the entire complex plane. The idea is that this greatly improves the control of the system, albeit with a larger number of optimization variables.

The target state is chosen to be a two-photon cat state, $\mathcal{N}(\left|\alpha = \sqrt{2}\right\rangle + \left|\alpha = -\sqrt{2}\right\rangle)$ with normalization constant $\mathcal{N}$. Below are the results of the optimization in the cases of different initial states. First, simply using the vacuum state $|0\rangle$ as initial state. Then, the two superpositions of Fock states $(|0\rangle + |1\rangle)/\sqrt{2}$ and $(|0\rangle + |2\rangle)/\sqrt{2}$ are used as initial states.

By setting the initial state to be the vacuum, $|0\rangle$, the optimizer found pulses that achieved $C_{opt} = 0.07819$ in $N_{iter} = 1135$ iterations. By applying the found pulses to the full Hamiltonian $\hat{H}_{N=6}$, the state overlap to the effective Hamiltonian is 0.97920, and the state overlap to the target state is 0.90463. The Wigner functions for the target state, as well as the simulated state using the found pulses for the full and effective Hamiltonians are shown in Figure 4.13.

To reach a cat state with the SNAIL-resonator, one idea is to try to trigger a number dependent displacement interaction. Essentially, by having an initial state of equal superpositions of Fock states, could see if the optimizer could find a way to evolve it into an equal superposition of coherent states. For the initial state $(|0\rangle + |1\rangle)/\sqrt{2}$, the optimizer found pulses that achieved $C_{opt} = 0.05093$ in $N_{iter} = 1500$ iterations. For those pulses, the state overlap between the full and effective Hamiltonians was 0.96945, and 0.93469 between the full Hamiltonian and the target state. The Wigner functions of the states simulated with the full and effective Hamiltonians are shown in Figure 4.14.

For the initial state $(|0\rangle + |2\rangle)/\sqrt{2}$, the optimizer reached the target cost with $C_{opt} = 0.00925$ after $N_{iter} = 276$ iterations. The state overlap between the full and effective Hamiltonian was 0.99638, and 0.98638 between the full Hamiltonian and the target state. It is important to note that there is a relatively large overlap between this initial state and the target state, $|\langle\psi_{target}|\psi_{init}\rangle|^2 \simeq 0.77460$.

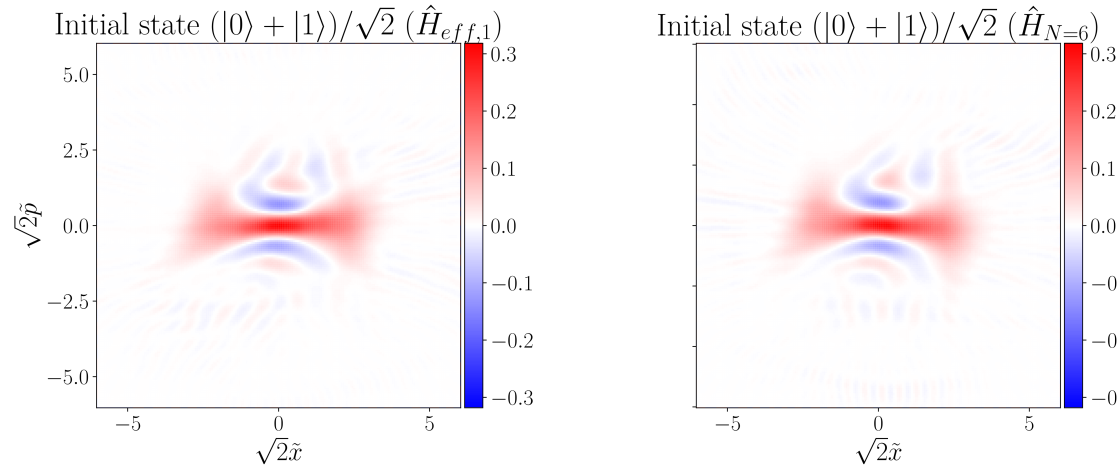

Figure 4.14: Wigner functions of the states generated by the shaped pulses for $\hat{H}_{\text{eff},1}$ (left) and $\hat{H}_{N=6}$ (right) with initial state $(|0\rangle + |1\rangle)/\sqrt{2}$, in a Hilbert space truncated at $N_{dim} = 100$.

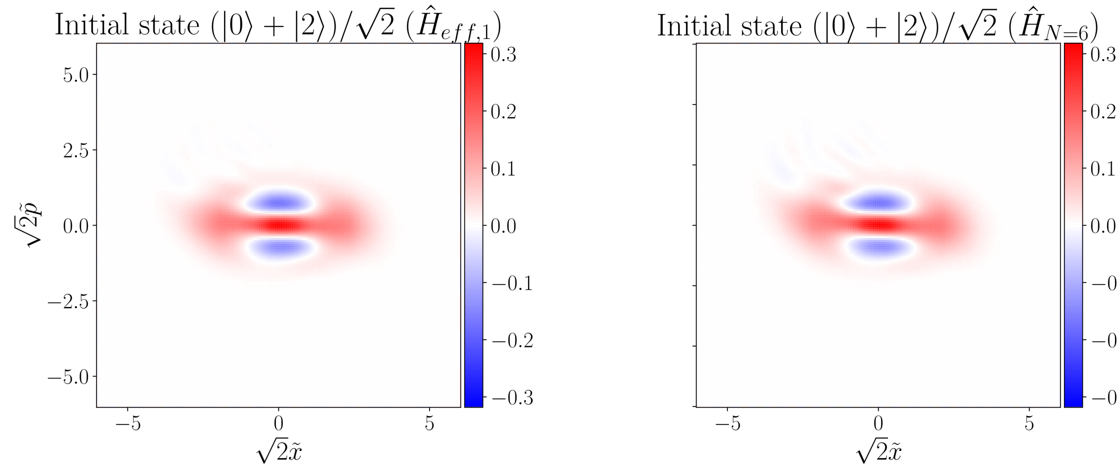

Figure 4.15: Wigner functions of the states generated by the shaped pulses for $\hat{H}_{\text{eff},1}$ (left) and $\hat{H}_{N=6}$ (right) with initial state $(|0\rangle + |2\rangle)/\sqrt{2}$, in a Hilbert space truncated at $N_{dim} = 100$.

5

Discussion

In this thesis, an effective Hamiltonian for the weakly and resonantly driven SNAIL-resonator has been derived, and then used for optimal control to generate cubic phase and cat states. The accuracy of this Hamiltonian compared to the full, time dependent Hamiltonian has been studied, and the performance of the optimal control methods has been evaluated. This will be the point of discussion for Section 5.1. Furthermore, the outlook for improving the optimal control of the SNAIL-resonator and extending it to different circuit architectures is discussed in Section 5.2.

5.1 Conclusion

From the simulations performed, one can conclude that the effective Hamiltonian in (4.9) and its corresponding micromotion operator in (4.10) emulate the full SNAIL-resonator Hamiltonian well in general. The major limitation to its accuracy is the amplitude of the applied flux pulses. In Fig. 4.5, one can see that it performs roughly 100 times better when the maximum amplitude is $0.010 \times 2\pi$ than for $0.030 \times 2\pi$. At these larger amplitudes, $\hat{H}_{M=2}$ becomes an increasingly worse approximation of $\hat{H}_{N=6}$, which in turn decreases the accuracy of $\hat{H}_{\text{eff},1}$ and $\hat{H}_{\text{eff},2}$. Hence, the first step of increasing the accuracy of the effective Hamiltonian further would be to derive it from $\hat{H}_{M=3}$ instead of $\hat{H}_{M=2}$.

On another note, the simulations also show that the first-order effective Hamiltonian, $\hat{H}_{eff,1}$, emulates $\hat{H}_{N=6}$ almost equally well for maximum amplitudes smaller than $0.010 \cdot 2\pi$. This Hamiltonian is much faster to simulate than the second-order Hamiltonian, simply due to requiring much fewer matrix multiplications. Hence, in order to speed up simulations, one can use this Hamiltonian instead when the amplitudes are sufficiently small. Alternatively, the simulation could be sped up by finding a fully analytical expression of $\hat{H}_{eff,2}$, as it has to be computed for each time t according to Appendix A.

The second limitation to the effective Hamiltonian is the rate of change of the pulse amplitudes. However, $\hat{H}_{eff,1}$ and $\hat{H}_{eff,2}$ emulated $\hat{H}_{N=6}$ well even when the rise time of the pulse decreased. The reason for this is likely that the pulse amplitudes are already required to be small, meaning that their rate of change is automatically small. In contrast, $\hat{H}_{M=2}$ performed worse in comparison to $\hat{H}_{N=6}$ for shorter rise times. This could be a direct effect of $\hat{H}_{M=2}$ being a worse approximation for higher amplitudes, as the pulse is at its maximum for longer when increasing the flat duration.

For the optimal control, it is shown that cubic phase states can be generated both by tuning the amplitude and phase of the pulses in [13], and by pulse shaping. Notably, for the case of pulse shaping the optimizer is never explicitly told that it is supposed to first squeeze the vacuum before applying a cubic phase gate. Instead it is given full freedom, and eventually finds a set of pulses that generate a higher fidelity cubic phase state than the tuned pulses when using $\hat{H}_{eff,1}$. However, it is also noteworthy that the overlap to the target state is smaller for the shaped pulses when using the full Hamiltonian $\hat{H}_{N=6}$. From the previous results in Section 4.1.4, one can deduce that this should be linked to the fact that the pulse amplitudes are large for a relatively long duration.

The study of robustness of the found pulses to deviations in Hamiltonian parameters show that both the standard and shaped pulses are generally robust towards such deviations. This shows some promise that the found pulses could be used successfully in experiment. However, to be certain about that one would need to study the robustness in more detail. For example, by studying larger deviations and by considering more deviations at the same time.

For generating cat states, the optimal control methods only proved to be somewhat effective. With $|0\rangle$ and $(|0\rangle+|1\rangle)/\sqrt{2}$ as initial states, the final cost in both cases was lower than 0.1, but still not very close to the target cost of 0.01. By examining their respective Wigner functions and comparing to that of the target state, it seems like the relatively low cost can be attributed to the similarity close to the origin. Hence, it remains unclear if a similarly low cost could be achieved for larger Fock states where more of the population is further from of the origin. With $(|0\rangle + |2\rangle)/\sqrt{2}$ as initial state, the optimizer reached the target cost relatively easily. However, the problem of achieving $(|0\rangle + |2\rangle)/\sqrt{2}$ in the first place still remains.

5.2 Outlook

There is still a lot of room for improvement for performing optimal control with the SNAIL-resonator. Firstly, it remains a question of how effective the optimal pulses would be in experiment. This is limited by three thing; the accuracy of the effective Hamiltonian to the full Hamiltonian, the accuracy of the full Hamiltonian to experiment, and the pulses' susceptibility against noise.

The accuracy of the effective Hamiltonian seems to be limited by the truncation of the ac-flux expansion, followed by the perturbative expansion order. Directly including higher-order terms would increase the computational cost of simulating the dynamics of the system, and hence slow down the optimization. In order to circumvent this, it is possible that one could find an analytically more compact form of the Hamiltonian to decrease the computational cost. The accuracy of the full Hamiltonian to experiment is limited by both uncertainty of the values of circuit parameters and the effect of the read-out qubit, which is not included in the Hamiltonian. From the results of this thesis, this does not seem to have a major effect on the performance of the optimal pulses. However, this needs to be investigated further to be certain. To mitigate this, one could either try to include the qubit's effect on the SNAIL-resonator in the Hamiltonian, or try to make the optimal pulses more robust to deviations in Hamiltonian parameters by altering the cost function. The pulses' susceptibility to noise could possibly be prevented by including the effects of noise in the simulation and ensuring that the pulses are robust towards it in the cost function.

Secondly, it is possible that the performance of the optimal control could be improved by using a different optimizer. Although using Boulder Opal is effective and convenient, there is not much freedom to tune the optimizer for a specific problem. Hence, it could be useful to perform the optimization using some other Python library, to allow for understanding what hinders the optimizer from reaching the target state and from that tune or change the optimizer accordingly.

Lastly, one may also have to consider what states are actually feasible to achieve with the SNAIL-resonator. Although the one is supposed to have universal control of its fundamental mode, there are remaining issues of noise and Kerr effects outside of the Kerr-free zone, which makes many interesting states unrealistic to achieve in this specific circuit architecture.

On another note, one could most likely extend the methods of optimal control to bosonic modes of other circuit architectures. One such architecture could be using an Asymmetrically Threaded Superconducting quantum interference device (ATS) [15] in place of the SNAIL. The ATS is similar to the SNAIL in its design, with an additional small JJ coupled in parallel. This extra arm creates a second loop in the circuit, which means it is possible to apply two separate flux biases to the device. This inherently gives an extra degree of freedom that can be used to suppress Kerr effects to a greater extent.

Bibliography

[1] C. D. Bruzewicz, J. Chiaverini, R. McConnell, and J. M. Sage, "Trapped-ion quantum computing: Progress and challenges," *Applied Physics Reviews*, vol. 6, no. 2, p. 21 314, May 2019, ISSN: 1931-9401. DOI: `10.1063/1.5088164`. [Online]. Available: `https://doi.org/10.1063/1.5088164`.

[2] C. Kloeffel and D. Loss, "Prospects for Spin-Based Quantum Computing in Quantum Dots," *Annual Review of Condensed Matter Physics*, vol. 4, no. Volume 4, 2013, pp. 51–81, 2013, ISSN: 1947-5462. DOI: `https://doi.org/10.1146/annurev-conmatphys-030212-184248`. [Online]. Available: `https://www.annualreviews.org/content/journals/10.1146/annurev-conmatphys-030212-184248`.

[3] M. H. Devoret and R. J. Schoelkopf, "Superconducting Circuits for Quantum Information: An Outlook," *Science*, vol. 339, no. 6124, pp. 1169–1174, Mar. 2013. DOI: `10.1126/science.1231930`. [Online]. Available: `https://doi.org/10.1126/science.1231930`.

[4] M. Kjaergaard, M. E. Schwartz, J. Braumüller, *et al.*, "Superconducting Qubits: Current State of Play," *Annual Review of Condensed Matter Physics*, vol. 11, pp. 369–395, 2020, ISSN: 19475462. DOI: `10.1146/annurev-conmatphys-031119-050605`.

[5] D. Gottesman, A. Kitaev, and J. Preskill, "Encoding a qubit in an oscillator," *Physical Review A*, vol. 64, no. 1, p. 12 310, Jun. 2001. DOI: `10.1103/PhysRevA.64.012310`. [Online]. Available: `https://link.aps.org/doi/10.1103/PhysRevA.64.012310`.

[6] W.-L. Ma, S. Puri, R. J. Schoelkopf, M. H. Devoret, S. M. Girvin, and L. Jiang, "Quantum control of bosonic modes with superconducting circuits," *Science Bulletin*, vol. 66, no. 17, pp. 1789–1805, 2021, ISSN: 2095-9273. DOI: `https://doi.org/10.1016/j.scib.2021.05.024`. [Online]. Available: `https://www.sciencedirect.com/science/article/pii/S2095927321004011`.

[7] R. Lescanne, M. Villiers, T. Peronnin, *et al.*, "Exponential suppression of bit-flips in a qubit encoded in an oscillator," *Nature Physics*, vol. 16, no. 5, pp. 509–513, 2020, ISSN: 1745-2481. DOI: `10.1038/s41567-020-0824-x`. [Online]. Available: `https://doi.org/10.1038/s41567-020-0824-x`.

[8] L. Hu, Y. Ma, W. Cai, *et al.*, "Quantum error correction and universal gate set operation on a binomial bosonic logical qubit," *Nature Physics*, vol. 15, no. 5, pp. 503–508, 2019, ISSN: 1745-2481. DOI: `10.1038/s41567-018-0414-3`. [Online]. Available: `https://doi.org/10.1038/s41567-018-0414-3`.

[9] R. W. Heeres, B. Vlastakis, E. Holland, *et al.*, "Cavity State Manipulation Using Photon-Number Selective Phase Gates," *Physical Review Letters*, vol. 115, no. 3, pp. 1–5, 2015, ISSN: 10797114. DOI: `10.1103/PhysRevLett.115.137002`.

[10] M. Kudra, M. Kervinen, I. Strandberg, *et al.*, "Robust Preparation of Wigner-Negative States with Optimized SNAP-Displacement Sequences," *PRX Quantum*, vol. 3, no. 3, p. 1, 2022, ISSN: 26913399. DOI: `10.1103/PRXQuantum.3.030301`. [Online]. Available: `https://doi.org/10.1103/PRXQuantum.3.030301`.

[11] A. Eickbusch, V. Sivak, A. Z. Ding, *et al.*, "Fast universal control of an oscillator with weak dispersive coupling to a qubit," *Nature Physics*, vol. 18, no. 12, pp. 1464–1469, 2022, ISSN: 17452481. DOI: `10.1038/s41567-022-01776-9`.

[12] M. Reagor, W. Pfaff, C. Axline, *et al.*, "Quantum memory with millisecond coherence in circuit QED," *Physical Review B*, vol. 94, no. 1, pp. 1–8, 2016, ISSN: 24699969. DOI: `10.1103/PhysRevB.94.014506`.

[13] A. M. Eriksson, T. Sépulcre, M. Kervinen, *et al.*, "Universal control of a bosonic mode via drive-activated native cubic interactions," *Nature Communications*, vol. 15, no. 1, p. 2512, 2024, ISSN: 2041-1723. DOI: `10.1038/s41467-024-46507-1`. [Online]. Available: `https://doi.org/10.1038/s41467-024-46507-1`.

[14] T. Hillmann, F. Quijandría, G. Johansson, A. Ferraro, S. Gasparinetti, and G. Ferrini, "Universal Gate Set for Continuous-Variable Quantum Computation with Microwave Circuits," *Physical Review Letters*, vol. 125, no. 16, p. 160 501, Oct. 2020. DOI: `10.1103/PhysRevLett.125.160501`. [Online]. Available: `https://link.aps.org/doi/10.1103/PhysRevLett.125.160501`.

[15] N. E. Frattini, U. Vool, S. Shankar, A. Narla, K. M. Sliwa, and M. H. Devoret, "3-wave mixing Josephson dipole element," *Applied Physics Letters*, vol. 110, no. 22, p. 222 603, May 2017, ISSN: 0003-6951. DOI: `10.1063/1.4984142`. [Online]. Available: `https://doi.org/10.1063/1.4984142`.

[16] P. T. Cochrane, G. J. Milburn, and W. J. Munro, "Macroscopically distinct quantum-superposition states as a bosonic code for amplitude damping," *Physical Review A*, vol. 59, no. 4, pp. 2631–2634, Apr. 1999. DOI: `10.1103/PhysRevA.59.2631`. [Online]. Available: `https://link.aps.org/doi/10.1103/PhysRevA.59.2631`.

[17] V. V. Albert, K. Noh, K. Duivenvoorden, *et al.*, "Performance and structure of single-mode bosonic codes," *Physical Review A*, vol. 97, no. 3, 2018, ISSN: 24699934. DOI: `10.1103/PhysRevA.97.032346`.

[18] A. Z. Ding, B. L. Brock, A. Eickbusch, *et al.*, "Quantum Control of an Oscillator with a Kerr-cat Qubit," 2024. [Online]. Available: `http://arxiv.org/abs/2407.10940`.

[19] A. Grimm, N. E. Frattini, S. Puri, *et al.*, "Stabilization and operation of a Kerr-cat qubit," *Nature*, vol. 584, no. 7820, pp. 205–209, 2020, ISSN: 14764687. DOI: `10.1038/s41586-020-2587-z`. [Online]. Available: `http://dx.doi.org/10.1038/s41586-020-2587-z`.

[20] X. L. He, Y. Lu, D. Q. Bao, *et al.*, "Fast generation of Schrödinger cat states using a Kerr-tunable superconducting resonator," *Nature Communications*, vol. 14, no. 1, 2023, ISSN: 20411723. DOI: `10.1038/s41467-023-42057-0`.

[21] S. Puri, S. Boutin, and A. Blais, "Engineering the quantum states of light in a Kerr-nonlinear resonator by two-photon driving," *npj Quantum Information*, vol. 3, no. 1, pp. 1–6, 2017, ISSN: 20566387. DOI: `10.1038/s41534-017-0019-1`. [Online]. Available: `http://dx.doi.org/10.1038/s41534-017-0019-1`.

[22] C. P. Koch, U. Boscain, T. Calarco, *et al.*, "Quantum optimal control in quantum technologies. Strategic report on current status, visions and goals for research in Europe," *EPJ Quantum Technology*, vol. 9, no. 1, p. 19, 2022, ISSN: 2196-0763. DOI: `10.1140/epjqt/s40507-022-00138-x`. [Online]. Available: `https://doi.org/10.1140/epjqt/s40507-022-00138-x`.

[23] Q. Ansel, E. Dionis, F. Arrouas, *et al.*, "Introduction to theoretical and experimental aspects of quantum optimal control," *Journal of Physics B: Atomic, Molecular and Optical Physics*, vol. 57, no. 13, 2024, ISSN: 13616455. DOI: `10.1088/1361-6455/ad46a5`.

[24] N. Khaneja, T. Reiss, C. Kehlet, T. Schulte-Herbrüggen, and S. J. Glaser, "Optimal control of coupled spin dynamics: design of NMR pulse sequences by gradient ascent algorithms," *Journal of Magnetic Resonance*, vol. 172, no. 2, pp. 296–305, 2005, ISSN: 1090-7807. DOI: `https://doi.org/10.1016/j.jmr.2004.11.004`. [Online]. Available: `https://www.sciencedirect.com/science/article/pii/S1090780704003696`.

[25] T. Caneva, T. Calarco, and S. Montangero, "Chopped random-basis quantum optimization," *Physical Review A*, vol. 84, no. 2, p. 22 326, Aug. 2011. DOI: `10.1103/PhysRevA.84.022326`. [Online]. Available: `https://link.aps.org/doi/10.1103/PhysRevA.84.022326`.

[26] P. Doria, T. Calarco, and S. Montangero, "Optimal Control Technique for Many-Body Quantum Dynamics," *Physical Review Letters*, vol. 106, no. 19, p. 190 501, May 2011. DOI: `10.1103/PhysRevLett.106.190501`. [Online]. Available: `https://link.aps.org/doi/10.1103/PhysRevLett.106.190501`.

[27] N. Rach, M. M. Müller, T. Calarco, and S. Montangero, "Dressing the chopped-random-basis optimization: A bandwidth-limited access to the trap-free landscape," *Physical Review A*, vol. 92, no. 6, p. 62 343, Dec. 2015. DOI: `10.1103/PhysRevA.92.062343`. [Online]. Available: `https://link.aps.org/doi/10.1103/PhysRevA.92.062343`.

[28] M. M. Müller, R. S. Said, F. Jelezko, T. Calarco, and S. Montangero, "One decade of quantum optimal control in the chopped random basis," *Reports on Progress in Physics*, vol. 85, no. 7, 2022, ISSN: 13616633. DOI: `10.1088/1361-6633/ac723c`.

[29] H.-P. Breuer and F. Petruccione, "The Theory of Open Quantum Systems," in *The Theory of Open Quantum Systems*, Oxford University Press, 2002, ch. 2.1, pp. 59–74.

[30] A. Blais, A. L. Grimsmo, S. M. Girvin, and A. Wallraff, "Circuit quantum electrodynamics," *Reviews of Modern Physics*, vol. 93, no. 2, p. 25 005, 2021, ISSN: 15390756. DOI: `10.1103/RevModPhys.93.025005`. [Online]. Available: `https://doi.org/10.1103/RevModPhys.93.025005`.

[31] U. Vool and M. Devoret, "Introduction to quantum electromagnetic circuits," *International Journal of Circuit Theory and Applications*, vol. 45, no. 7, pp. 897–934, 2017, ISSN: 1097007X. DOI: `10.1002/cta.2359`.

[32] I. I. Rabi, J. R. Zacharias, S. Millman, and P. Kusch, "A New Method of Measuring Nuclear Magnetic Moment," *Physical Review*, vol. 53, no. 4, p. 318, Feb. 1938. DOI: `10.1103/PhysRev.53.318`. [Online]. Available: `https://link.aps.org/doi/10.1103/PhysRev.53.318`.

[33] D. Burgarth, P. Facchi, R. Hillier, and M. Ligabò, "Taming the Rotating Wave Approximation," *Quantum*, vol. 8, p. 1262, 2024, ISSN: 2521-327X. DOI: `10.22331/q-2024-02-21-1262`. [Online]. Available: `https://doi.org/10.22331/q-2024-02-21-1262`.

[34] M. Mirrahimi and P. Rouchon, *Dynamics and Control of Open Quantum Systems*, 2015. [Online]. Available: `https://who.rocq.inria.fr/Mazyar.Mirrahimi/QuantSys2015.pdf`.

[35] J. Venkatraman, X. Xiao, R. G. Cortiñas, A. Eickbusch, and M. H. Devoret, "Static Effective Hamiltonian of a Rapidly Driven Nonlinear System," *Physical Review Letters*, vol. 129, no. 10, p. 100 601, Aug. 2022. DOI: `10.1103/PhysRevLett.129.100601`. [Online]. Available: `https://link.aps.org/doi/10.1103/PhysRevLett.129.100601`.

[36] F Casas, J A Oteo, and J Ros, "Floquet theory: exponential perturbative treatment," *Journal of Physics A: Mathematical and General*, vol. 34, no. 16, p. 3379, 2001, ISSN: 0305-4470. DOI: `10.1088/0305-4470/34/16/305`. [Online]. Available: `https://dx.doi.org/10.1088/0305-4470/34/16/305`.

[37] A. Eckardt, "Colloquium: Atomic quantum gases in periodically driven optical lattices," *Reviews of Modern Physics*, vol. 89, no. 1, p. 11 004, Mar. 2017. DOI: `10.1103/RevModPhys.89.011004`. [Online]. Available: `https://link.aps.org/doi/10.1103/RevModPhys.89.011004`.

[38] W. Shao, C. Wu, and X.-L. Feng, "Generalized James' effective Hamiltonian method," *Physical Review A*, vol. 95, no. 3, p. 32 124, Mar. 2017. DOI: `10.1103/PhysRevA.95.032124`. [Online]. Available: `https://link.aps.org/doi/10.1103/PhysRevA.95.032124`.

[39] T. Hillmann and F. Quijandría, "Designing Kerr Interactions for Quantum Information Processing via Counterrotating Terms of Asymmetric Josephson-Junction Loops," *Physical Review Applied*, vol. 17, no. 6, p. 64 018, Jun. 2022. DOI: `10.1103/PhysRevApplied.17.064018`. [Online]. Available: `https://link.aps.org/doi/10.1103/PhysRevApplied.17.064018`.

[40] J. J. Sakurai and J. Napolitano, *Modern Quantum Mechanics*, 3rd ed. Cambridge University Press, 2021, pp. 62–148, ISBN: 978-1-108-47322-4.

[41] J. R. Johansson, P. D. Nation, and F. Nori, "QuTiP 2: A Python framework for the dynamics of open quantum systems," *Computer Physics Communications*, vol. 184, no. 4, pp. 1234–1240, 2013, ISSN: 0010-4655. DOI: `https://doi.org/10.1016/j.cpc.2012.11.019`. [Online]. Available: `https://www.sciencedirect.com/science/article/pii/S0010465512003955`.

[42] Q-CTRL, *Boulder Opal*, 2025. [Online]. Available: `https://q-ctrl.com/boulder-opal`.

[43] N. Hansen, "The CMA Evolution Strategy: A Tutorial," pp. 1–39, 2016. [Online]. Available: `http://arxiv.org/abs/1604.00772`.

A

Definition of Rotating Terms in Hamiltonian

Here, the effective Hamiltonian and its corresponding micromotion operator are thoroughly defined for an applied set of pulses

$$\xi(t) = \sum_m v_m(t)\cos(\omega_0 t + \gamma_m), \tag{A.1a}$$

$$\phi_e^{\mathrm{ac}}(t) = \sum_{n=1}^{3}\sum_m u_{n,m}(t)\cos(n\omega_0 t + \theta_{n,m}), \tag{A.1b}$$

where $v_m(t)$ and $u_{n,m}(t)$ are slowly varying pulse envelopes. First, remember that the truncated Hamiltonian can be written in the frame rotating with ω_0 as

$$\begin{aligned}\hat{H}_I(t) = {} & \xi(t)(\hat{a}^\dagger e^{i\omega_0 t} + \hat{a}e^{-i\omega_0 t}) + \\ & + \sum_{k=1}^{6}(g_k^{\mathrm{dc}} + g_{k,1}^{\mathrm{ac}}\phi_e^{\mathrm{ac}}(t) + g_{k,2}^{\mathrm{ac}}\phi_e^{\mathrm{ac}}(t)^2)(\hat{a}^\dagger e^{i\omega_0 t} + \hat{a}e^{-i\omega_0 t})^k,\end{aligned} \tag{A.2}$$

which can be rewritten as

$$\hat{H}_I(t) = \sum_{k=-12}^{12}\hat{h}_k(t)e^{ik\omega_0 t}, \tag{A.3}$$

where $\hat{h}_k(t)$ are slowly varying in time along with the drive amplitudes. Starting with the flux drive part of the full Hamiltonian in the rotating frame,

$$\sum_{k'=1}^{6}(g_{k'}^{\mathrm{dc}} + g_{k',1}^{\mathrm{ac}}\phi_e^{\mathrm{ac}}(t) + g_{k',2}^{\mathrm{ac}}\phi_e^{\mathrm{ac}}(t)^2)(\hat{a}^\dagger e^{i\omega_0 t} + \hat{a}e^{-i\omega_0 t})^{k'}, \tag{A.4}$$

one can redefine

$$\sum_{k'=1}^{6}(g_{k'}^{\mathrm{dc}} + g_{k',1}^{\mathrm{ac}}\phi_e^{\mathrm{ac}}(t) + g_{k',2}^{\mathrm{ac}}\phi_e^{\mathrm{ac}}(t)^2) \equiv \sum_{j=-6}^{6} f_j(t)e^{ij\omega_0 t}, \tag{A.5}$$

where $f_j(t)$ varies with the pulse amplitudes. This gives

$$f_0(t) = \sum_{k'=1}^{6} \left(g_{k'}^{\mathrm{dc}} + g_{k',2}^{\mathrm{ac}} \sum_{n=1}^{3} \sum_{m,m'} \frac{u_{n,m}(t) u_{n,m'}(t)}{2} \cos(\theta_{n,m} - \theta_{n,m'}) \right), \tag{A.6a}$$

$$\begin{aligned} f_1(t) = \sum_{k'=1}^{6} \Bigg(&\sum_{m} \frac{g_{k',1}^{\mathrm{ac}} u_{1,m}(t)}{2} e^{i\theta_{1,m}} + \\ &+ g_{k',2}^{\mathrm{ac}} \sum_{m'} \frac{u_{2,m}(t) u_{1,m'}(t)}{2} e^{i(\theta_{2,m} - \theta_{1,m'})} + \frac{u_{3,m}(t) u_{2,m'}(t)}{2} e^{i(\theta_{3,m} - \theta_{2,m'})} \Bigg), \end{aligned} \tag{A.6b}$$

$$\begin{aligned} f_2(t) = \sum_{k'=1}^{6} \Bigg(&\sum_{m} \frac{g_{k',1}^{\mathrm{ac}} u_{2,m}(t)}{2} e^{i\theta_{2,m}} + \\ &+ g_{k',2}^{\mathrm{ac}} \sum_{m'} \frac{u_{3,m}(t) u_{1,m'}(t)}{2} e^{i(\theta_{3,m} - \theta_{1,m'})} + \frac{u_{1,m}(t) u_{1,m'}(t)}{4} e^{i(\theta_{1,m} + \theta_{1,m'})} \Bigg), \end{aligned} \tag{A.6c}$$

$$\begin{aligned} f_3(t) = \sum_{k'=1}^{6} \Bigg(&\sum_{m} \frac{g_{k',1}^{\mathrm{ac}} u_{3,m}(t)}{2} e^{i\theta_{3,m}} + \\ &+ g_{k',2}^{\mathrm{ac}} \sum_{m'} \frac{u_{2,m}(t) u_{1,m'}(t)}{2} e^{i(\theta_{2,m} + \theta_{1,m'})} \Bigg), \end{aligned} \tag{A.6d}$$

$$\begin{aligned} f_4(t) = \sum_{k'=1}^{6} \Bigg(&g_{k',2}^{\mathrm{ac}} \sum_{m,m'} \frac{u_{3,m}(t) u_{1,m'}(t)}{2} e^{i(\theta_{3,m} + \theta_{1,m'})} + \\ &+ \frac{u_{2,m}(t) u_{2,m'}(t)}{4} e^{i(\theta_{2,m} + \theta_{2,m'})} \Bigg), \end{aligned} \tag{A.6e}$$

$$f_5(t) = \sum_{k'=1}^{6} g_{k',2}^{\mathrm{ac}} \sum_{m,m'} \frac{u_{3,m}(t) u_{2,m'}(t)}{2} e^{i(\theta_{3,m} + \theta_{2,m'})}, \tag{A.6f}$$

$$f_6(t) = \sum_{k'=1}^{6} g_{k',2}^{\mathrm{ac}} \sum_{m,m'} \frac{u_{3,m}(t) u_{3,m'}(t)}{4} e^{i(\theta_{3,m} + \theta_{3,m'})}. \tag{A.6g}$$

For $j = -1, ..., -6$, it is enough to realize that $f_{-j}(t) = f_j(t)^*$. After this, one can split each of these functions into six parts, each representing one part of the sum $\sum_{k'=1}^{6}$, such that $f_j(t) = \sum_{k'=1}^{6} f_j^{[k']}(t)$. To demonstrate, this gives e.g.

$$f_0^{[3]}(t) = g_3^{\mathrm{dc}} + g_{3,2}^{\mathrm{ac}} \sum_{n=1}^{3} \sum_{m,m'} \frac{u_{n,m}(t) u_{n,m'}(t)}{2} \cos(\theta_{n,m} - \theta_{n,m'}). \tag{A.7}$$

Next, one can define $\hat{A}_j^{[k']}$ such that

$$(\hat{a}^\dagger e^{i\omega_0 t} + \hat{a} e^{-i\omega_0 t})^{k'} \equiv \sum_{j=-6}^{6} \hat{A}_j^{[k']} e^{ij\omega_0 t}. \tag{A.8}$$

This gives

$$\hat{A}_0^{[2]} = 2\hat{a}^\dagger\hat{a},\ \hat{A}_0^{[4]} = 12\hat{a}^\dagger\hat{a} + 6\hat{a}^{\dagger 2}\hat{a}^2,\ \hat{A}_0^{[6]} = 90\hat{a}^\dagger\hat{a} + 90\hat{a}^{\dagger 2}\hat{a}^2 + 20\hat{a}^{\dagger 3}\hat{a}^3, \tag{A.9a}$$

$$\hat{A}_1^{[1]} = \hat{a}^\dagger,\ \hat{A}_1^{[3]} = 3\hat{a}^\dagger + 3\hat{a}^{\dagger 2}\hat{a},\ \hat{A}_1^{[5]} = 15\hat{a}^\dagger + 30\hat{a}^{\dagger 2}\hat{a} + 10\hat{a}^{\dagger 3}\hat{a}^2, \tag{A.9b}$$

$$\hat{A}_2^{[2]} = \hat{a}^{\dagger 2},\ \hat{A}_2^{[4]} = 6\hat{a}^{\dagger 2} + 4\hat{a}^{\dagger 3}\hat{a},\ \hat{A}_2^{[6]} = 45\hat{a}^{\dagger 2} + 60\hat{a}^{\dagger 3}\hat{a} + 15\hat{a}^{\dagger 4}\hat{a}^2, \tag{A.9c}$$

$$\hat{A}_3^{[3]} = \hat{a}^{\dagger 3},\ \hat{A}_3^{[5]} = 10\hat{a}^{\dagger 3} + 5\hat{a}^{\dagger 4}\hat{a}, \tag{A.9d}$$

$$\hat{A}_4^{[4]} = \hat{a}^{\dagger 4},\ \hat{A}_4^{[6]} = 15\hat{a}^{\dagger 4} + 6\hat{a}^{\dagger 5}\hat{a}, \tag{A.9e}$$

$$\hat{A}_5^{[5]} = \hat{a}^{\dagger 5}, \tag{A.9f}$$

$$\hat{A}_6^{[6]} = \hat{a}^{\dagger 6}. \tag{A.9g}$$

Again, for $j = -1, ..., -6$, one can notice that $\hat{A}_{-j}^{[k']} = \hat{A}_j^{[k']\dagger}$. The remaining operators not written above are equal to zero.

Now, each part of the rotated Hamiltonian can be expressed as

$$\hat{h}_k(t) = \sum_{j+j'=k} \sum_{k'=1}^{6} f_j^{[k']}(t)\hat{A}_{j'}^{[k']}(t), \tag{A.10}$$

and hence the entire Hamiltonian in the rotating frame can be written as

$$\hat{H}_I(t) = \sum_{k=-12}^{12} \sum_{j+j'=k} \sum_{k'=1}^{6} f_j^{[k']}(t)\hat{A}_{j'}^{[k']}(t)e^{ik\omega_0 t}. \tag{A.11}$$

From this, it is also evident that $\hat{h}_k(t)^\dagger = \hat{h}_{-k}(t)$.

The effective Hamiltonian and its corresponding micromotion operator are then given by

$$\hat{H}_{\text{eff}}(t) = \hat{h}_0 + \sum_{k\neq 0}\left(\frac{\left[\hat{h}_k, \hat{h}_{-k}\right]}{2k\omega_0} + \frac{\left[\left[\hat{h}_k, \hat{h}_0\right], \hat{h}_{-k}\right]}{2k^2\omega_0^2} + \sum_{l\neq k,0}\frac{\left[\left[\hat{h}_l, \hat{h}_{k-l}\right], \hat{h}_{-k}\right]}{3kl\omega_0^2}\right), \tag{A.12}$$

$$\hat{S}(t) = i\sum_{k\neq 0}\left(\frac{\hat{h}_k}{k\omega_0} + \frac{\left[\hat{h}_k, \hat{h}_0\right]}{k^2\omega_0^2} + \sum_{l\neq k,0}\frac{\left[\hat{h}_l, \hat{h}_{k-l}\right]}{2kl\omega_0^2}\right)e^{ik\omega_0 t}, \tag{A.13}$$

where the slow time-dependence of each $\hat{h}_k(t)$ is omitted to simplify the notation.

DEPARTMENT OF MICROTECHNOLOGY AND NANOSCIENCE
CHALMERS UNIVERSITY OF TECHNOLOGY
Gothenburg, Sweden
www.chalmers.se

CHALMERS
UNIVERSITY OF TECHNOLOGY